Contrasting granitic magmatism of the Kalba fold belt (East Kazakhstan): evidence for Late Paleozoic post-orogenic events

M.L. Kuibida[a,b,*], B.A. Dyachkov[c], A.G. Vladimirov[a,b], N.N. Kruk[a,b], S.V. Khromykh[a,b], P.D. Kotler[a,b], S.N. Rudnev[a], E.A. Kruk[a], Y.V. Kuibida[a], T. Oitseva[c]

a – Sobolev Institute of Geology and Mineralogy SB RAS, Koptyuga ave. 3, Novosibirsk, 630090, Russia

b – Novosibirsk State University, Pirogova st. 2, Novosibirsk, 630090, Russia

c – East-Kazakhstan State Technical University, Serikbayeva st.19, Ust'-Kamenogorsk, 070010, Kazakhstan

ABSTRACT

The paper presents new original data and a review of previous studies on the Late Carboniferous – Early Permian granitoids of the Kunush and Kalguty intrusive complexes from the Kalba fold belt (East Kazakhstan). These rocks formed at the initial post-collisional stage of the Irtish-Zaisan orogen in the western Central Asian Orogenic Belt (CAOB). The granitoids form isometric or NW linear intrusions inside the Late Devonian - Early Carboniferous metasediments which overlap the accretionary lithology of the Kalba fold belt in front of the Altai active margin of the Siberian continent. These granitoids contain zircon grains with U-Pb ages of ca.308-291 Ma, synchronous with the peak post-orogenic magmatic event at ~300 Ma in the CAOB. The Kunush high-Na granitoids, with high SiO_2 (67–72%) and Al_2O_3 (15–18%) contents and the Na_2O/K_2O ratio (1.94–6.43), and low HREEs (Yb = 0.22–0.93 ppm) but moderate Sr/Y ratios (47–179), *Mg#* (35–55) and Ni, Cr, are generally common to high-Al TTG-series with non-subduction geochemical signatures. The Kalguty granitoids mostly belong to calc-alkalic to subalkalic high-K series, have non-corundum CIPW-norm compositions and mainly weakly peraluminous (*ASI* = 0.97–1.09) characteristics. Their *Fe** = 0.7-1 at 62-74 wt.% SiO_2 and relatively high Y/Nb (2-4) and Rb/Nb (9-18) ratios

are similar to transitional compositions reported for fractionated *I*- and A_2-type post-orogenic granites worldwide. The Kunush high-Na and Kalguty high-K granitoids formed at different depths in the crust and the parent melts were derived from metabasaltic (MORB; P = 10-15 kbar) and metagranitic (TTG-like; P < 10 kbar) protoliths, respectively. We propose that relaxation of tangential compression after oblique collision and the following thermal impact of mafic magma that acted simulataneously at different crustal depths, along with decompressional partial melting, may be a basic petrological scenario for synchronous formation of geochemically different granitoids.

Key words: post-collision magmatism, hot shear system, Kunush-Kalguty granitoids, Irtysh-Zaisan orogen, Central Asian Orogenic Belt.

1. Introduction

Post-orogenic magmatic rocks are widespread in the world (Collins et al., 1982; Sylvester, 1989, 1998; Whalen et al., 1996). Magmatism was commonly initiated in within-plate tectonic settings, ~25 Mys after oceanic suturing, at continuing horizontal motions of previously accreted terranes: thrusting, terrane rotation, strike-slip faulting, shearing and rifting (Sylvester, 1989; Black and Liégeois, 1993; Holister et al., 1993; Liégeois et al., 1998; Ferre et al., 1998). Post-orogenic magmatism is often attributed to slab break-off and subsequent delamination of subcontinental lithospheric mantle, asthenospheric upwelling and magmatic underplating, accompanied by exhumation of high-grade metamorphic crust (e.g. Dawey, 1988, Kay and Kay, 1993; Davies and von Blanckenburg, 1995). The ascent of asthenospheric diapirs induces rapid heating and anatexis of the continental crust, interaction between mantle- and crust-derived melts, and generation of compositionally diverse and isotope hybrid granitoids.

Post-orogenic felsic magmatism is known from the regions of Alaska, Cordillera, Lachlan and New England (Australia) accretionary-collisional orogenic belts, and in the

Arabian-Nubian Shield, as summarized and classified by Sylvester (1989). The granitoids mostly belong to moderate- or high-K calc-alkaline and shoshonitic series (syenite, monzonite and quartz-monzonite, and monzogranite) but some also have calc-alkaline quartz-diorite and tonalite-granodiorite compositions with geochemical features similar to felsic magmatism of volcanic arc and syn-orogenic setting (Harris et al., 1986). There is also clear evidence of a coeval generation of crust-derived adakite-like and alkaline granitoids in course intra-continental extension of overthickened metamorphic crust (Zhao et al., 2016). In the paper we define the term "contrasting granitic magmatism" as the association of granitoids with divergent geochemical signatures of felsic magmatism of a thickened orogen and a post-orogenic extension setting. We operate a simple idea that granitoids are an important "witness" of global deep dynamic events because generation of felsic magma requires a powerful source of heat to melt crustal material. The isotope age of synchronous contrasting granitoids can trace the time of tectonic setting changes.

The most prominent examples of post-orogenic magmatism come from the Late Paleozoic extension settings of Central Asia. The Central Asian Orogenic Belt (CAOB), or the Altaid Tectonic Collage (Altaids), is the world largest accretionary area, a Pacific-type system that comprises multiple subduction-accretionary orogens (e.g., Zonenshain et al., 1990; Mossakosky et al., 1993; Şengör et al., 1993; Dobretsov et al., 1995; Jahn et al., 2000; Yakubchuk, 2004; Buslov et al., 2004; Windley et al., 2007; Xiao et al., 2010; Safonova et al., 2011; Kröner et al., 2014; Xiao and Santosh, 2014; Chen et al., 2017; Safonova et al., 2018a). The western COAB segment extends for more than 2500 km from the Russian Ural in the west, across Eastern Kazakhstan and Northwest China to Southern Mongolia. It formed in the late Neoproterozoic – Late Paleozoic by closure and suturing of the Paleo-Asian Ocean (PAO) which once separated the Siberian Craton from the Tarim, North China and Kazakhstan continents. The PAO history continued for more than 800 mys and included multiple events of subduction and accretion of oceanic island/plateau, island-arc, and

microcontinent terranes, of both western Pacific- and Andean-type styles, which had eventually amalgamated into the CAOB in the Late Palaeozoic.

This is, specifically, the Irtysh-Zaisan orogen that formed at the junction of Siberia and Kazakhstan during closure of the PAO (Fig. 1). The Kalba fold belt, one of the major constituents of the Irtysh-Zaisan orogen, formed in front of the Altai active margin in the Early Carboniferous, after transpression of the Irtysh-Zaisan oceanic plate, in the course of complex amalgamating of Siberian and Kazakhstan continents (e.g., Konnikov et al., 1977; Yermolov et al., 1983; Shcherba et al., 1998; Buslov et al., 2001; Vladimirov et al., 2008). The study of the Late Paleozoic magmatism of the Kalba fold belt provides important insights into post-collisional processes during the formation of western CAOB. In addition, the granitic intrusions have similar spatial and structural relations with gold and rare metal mineralization. However, the age and origin of this magmatism remains a subject of discussion.

2. Tectonic setting and geological framework

The Kalba fold belt is a ca. 70-100 km wide and above 300 km long zone extended from south-east to north-west over the entire in East Kazakhstan segment of the Irtysh-Zaisan orogen (Fig. 1). Geophysical data (Shcherba et al., 1998) reveal a highly anisotropic structure and heterogeneous crust lithology in the Kalba fold belt composed of voluminous metasediments lying over tectonic mélange (metagreywacke and metabasalt); all these rocks were altered by tectonic burial and exhumation from lower-middle crustal depths (Shcherba et al., 1998; Hu et al., 2000; Briggs et al., 2007; Ermolov, 2013). The present continental crust is as thick as 47$\pm$6 km and consists of an 18-26 km thick granitic layer lying over a 14-18 km basaltic layer (Shcherba et al., 1998).

The Kalba fold belt is intruded by voluminous Early Permian granitoids, such as the well documented the giant Kalba-Narym batholith reaching a size of 11400 km^3 (Kuzebny,

1975; Lopatnikov et al., 1982; Shcherba et al., 1998; Vladimirov et al., 2001, 2003, 2008; Kotler et al., 2015; Khromykh et al., 2016). There are also smaller (2500 km^3) Late Carboniferous intrusions of the Kunush and Kalguty intrusive complexes and their dykes, which emplaced before the main batholith (D'yachkov, 1972; D'yachkov et al., 1994). The Kunush and Kalguty granitoids intruded into Late Devonian black schists, Early Carboniferous turbidite and greywacke lithology, and Moscovian molasse and were, in their turn, intruded by Permian granitic batholiths. The Kunush intrusions emplaced along steeply dipping regional faults, which make up a 20 to 25 km wide fault zone extending for 80 to 120 km, according to north-west orientation of the Kalba fold belt (Lopatnikov et al., 1982; Fig. 1). The Kunush granitoids underwent syn-deformational mylonitization. Unlike these, the Kalguty granitoids occupied fault intersections and thus avoided significant deformation. The main granitic phases form stocks and linear intrusions, from 0.05 to 3 km in size or 0.1-3 km^2 (Fig. 2). The dykes are stratified steeply dipping bodies, 2 to 10 m wide and 1 to 3 km long, which are located away from the main intrusions and obviously result from several events. No intrusive contacts between the main granitic phases of the Kunush and Kalguty intrusive complexes have been found, but high-Na granitic dykes cut through the high-K dykes. The Kunush fine-grained granite cuts through the Kalguty rocks in the Razdolny intrusion and is younger than other Kunush granitoids (see Section 4.1).

The Kunush complex includes massive, porphyritic and fine-grained granitoids and granite-porphyry which have been studied in the Zhilandy, Tochka, Besterek and Razdolny intrusions and in the Kunush-dyke (dyke near the Kunush intrusion). The Kalguty plutonic rocks were previously identified as granodiorite (Lopatnikov et al., 1982), but we classify them as quartz-monzonite, monzogranite and granodiorites, in this study. The granitoids were studied (Fig. 1) in the Kurchum and Razdolny intrusions and in the VDN-dyke (VDN is a Russian abbreviation of the Navozov Greate Dyke).

3. Analytical methods

3.1. Zircon U-Pb dating

The cathodoluminescence images of zircons and the results of $^{206}Pb/^{238}U$ dating are shown in Table 1 and Figs. 3, 4. The U–Pb geochronological studies were performed by the LA-SF-ICP-MS method on a Thermo Fisher Scientific *Element XR* high-resolution mass spectrometer with a *New Wave Research UP-213* laser ablation system, at the Geological Institute (Ulan-Ude), as in (Khubanov et al., 2016). The analysis was applied to 20–50 single zircon grains, similar in morphology and size in each sample, which were embedded in epoxy resin together with TEMORA-II and Plešovice standard zircons.

The zircon grains were cut off to about a half of their thickness and polished. The dating points on the grain surfaces were selected using optical and SEM images. The zircons were irradiated by a pulse laser beam (40 μm diameter) at 10 Hz for 30 s. The evaporated particles were carried from the laser system to the mass spectrometer in a stream of pure He. The *Glitter* software (Griffin et al., 2008) was used for drift correction of the measured isotopes, with regard to the background signals, and for calculating isotope ratios and their errors. The data were processed using the *ISOPLOT* software (Ludwig et al., 2003). Four isotope ratios were measured: $^{207}Pb/^{206}Pb$, $^{206}Pb/^{238}U$, $^{207}Pb/^{235}U$ and $^{208}Pb/^{232}Th$, but no total lead correction was applied. The age was calculated according to the position of U-Pb ratios ($^{206}Pb/^{238}U$–$^{207}Pb/^{235}U$) in the concordia diagram. The isotope ratios were measured to 1σ errors of ~1.5 % for $^{206}Pb/^{238}U$ and 4-5 % for $^{207}Pb/^{235}U$ in standard zircons, which is approximately commensurate with the respective errors in the SHRIMP method. The CL imaging was performed at the Novosibirsk Institute Geology and Mineralogy using a Jeol *JSM-6510LV* scanning electron microscope. The locations for the spot analysis on zircon grains were selected from CL images and photomicrographs, in transmitted and reflected light, to avoid mineral inclusions and cracks.

3.2. Whole-rock compositions

The concentrations of major elements were measured by a *CMP-25* X-ray fluorescence (XRF) device according to the state standard of the USSR Ministry of Geology (GOST 41-08-212-82) at the Institute of Geology and Mineralogy (IGM, Novosibirsk). Trace elements were determined by the inductively coupled plasma mass spectrometry (ICP-MS) on a *Finnigan Element* ICP-MS analyzer, at IGM, following the protocols of Jenner et al. (1990). Powdered samples were digested in a HF-HNO_3 (2:1) mixture in a screw-top *Teflon* beaker for 2 days at ~100 °C, then evaporated to dryness, refluxed in 6N HCl and dried twice, and then redissolved in 1N HCl. The procedure was repeated till complete dissolution of the powder. The final solution was evaporated to dryness, refluxed in 6N HNO_3, dried three times, and dissolved in 2% HNO_3. The wet chemistry analytical work was conducted under clean lab conditions. The precision and accuracy of the analyses were checked against the BHVO-1 (Jenner et al., 1990), BCR-1 (Jochum and Nohl, 2008), and JB-3 (Orihashi and Hirata, 2003) international standards and estimated to be 2–7% for rare earth and high-field strength elements. The element abundances and ratios were normalized to chondritic (e.g., La/Sm_n) and primitive mantle (PM) values (e.g., Th/Nb_{pm}), with reference to Sun and McDonough (1989) and McDonough et al. (1992), respectively. Representative analyses of major and trace element contents (in wt.% and ppm, respectively) are given in Tables 2 and 3.

3.3. Isotopes

Radiogenic Sm-Nd isotope studies were carried out for bulk samples at the Geological Institute of the Kola Science Center (Apatity) on a *Finnigan* MAT 262 (RPQ) seven-channel solid-state mass spectrometer. Isotope ratios were normalized to $^{146}Nd/^{144}Nd = 0.7219$ and then recalculated for the $^{143}Nd/^{144}Nd = 0.511860$ ratio assumed for the *La Jolla* Nd standard, with a $^{143}Nd/^{144}Nd$ weight average ratio of 0.511837 ± 12 (2σ), from 36 measurements. The $\varepsilon Nd(t)$ values and model ages T_{DM} were calculated with reference to $^{143}Nd/^{144}Nd=0.512638$

and $^{147}Sm/^{144}Nd$=0.1967 (Jacobsen and Wasserburg, 1984) and the respective depleted mantle (DM) ratios of $^{143}Nd/^{144}Nd$ = 0.513151 and $^{147}Sm/^{144}Nd$=0.2136 (Goldstein and Jacobsen, 1988). Two-stage age models T_{DM-2} were obtained assuming a middle crust ratio of $^{147}Sm/^{144}Nd$ = 0.12 (Liew and Hofman, 1998). Sm–Nd isotopic data are presented in Table 4; all errors quoted in this paper are 2σ. All the εNd(t) values of the Kunush and Kalguty granitoids have been calculated using the average U–Pb age of 300 Ma.

4. Results

4.1. Zircon U-Pb geochronology

U-Pb dating of zircons from samples of the Kalguty massive quartz-monzonite (X-1052, X-1047, Kurchum), granodiorite (MX-841, Razdolny), quartz-monzonite porphyry (KT-34/1, VDN-dyke), and Kunush porphyritic granite (K-14-104, Besterek) and granite porphyry (7-694, dyke near the Kunush intrusion), respectively, provided time constraints on the emplacement of the Kalguty and Kunush intrusive complexes in the Kalba fold belt.

4.1.1. Kalguty intrusive complex

The $^{206}Pb/^{238}U$ age of the Kalguty complex was obtained for two quartz-monzonitic samples of early and late phases of the Kurchum intrusion. The zircon grains of X-1052 selected for LA-SF-ICP-MS U–Pb dating are colorless or pale yellow euhedral prismatic crystals (80–350 μm, K_L = 2–4), with oscillatory zoning indicating magmatic origin detectable in cathodoluminescence (CL) images (Fig. 3a). Some zircons have distinct cores, which may be relict zircons inherited from previous events. A concordant $^{206}Pb/^{238}U$ age of 308±2 Ma (MSWD=0.41) was obtained from 44 analyses of local spots in different parts of zoned magmatic crystals (Nos. 1-44 in Table 1) and interpreted as the age of emplacement (Fig. 4a). The zircons of X-1047 are colorless or pale yellow or pinkish euhedral prismatic crystals (80-270 μm, K_L = 2–3.5 or 5-6 in some cases), likewise with thin oscillatory zoning (Fig. 3b).

Some crystals enclose inherited relict zircon grains at the core. The emplacement time corresponds to concordant $^{206}Pb/^{238}U$ ages of 303±2 Ma (MSWD=0.68) based on 31 analyses (Nos. 45-75 in Table 1); Fig. 4b.

The Razdolny intrusion was previously considered as age analog of the late phase of the Kurchum intrusion. Its age was determined for samples of the main intrusive phase. Zircon grains of MX-841 isolated for LA-SF-ICP-MS U–Pb dating are colorless or pale yellow euhedral prismatic crystals (40–180 μm, K_L = 2–5), with coarse oscillatory zoning in CL images, and with relict xenogenic zircons in some cases (Fig. 3c). The results of 24 analyses (Nos. 76-99 in Table 1) gave a concordant $^{206}Pb/^{238}U$ age of 291±2 Ma (MSWD = 2.0) (Fig. 4c).

The VDN-dyke quartz-monzonite porphyry was analyzed to determine the age of the high-K dyke series. Zircons from K-34/1 isolated for LA-SF-ICP-MS U–Pb dating are transparent colorless or light-yellow euhedral prismatic crystals (100-450 μm, K_L = 2.0–4.5, in some cases 6), with clear oscillatory magmatic zoning in CL images (Fig. 3d). The isotopic ratios $^{206}Pb/^{238}U$ for these points (Fig. 4d) give a concordant age of 306±2 Ma (MSWD = 1.8) based on 22 analyses (Nos. 100-121 in Table 1).

4.1.2. Kunush intrusive complex

The $^{206}Pb/^{238}U$ ages of massive (307 Ma, Zhilandy, sample 7-181) and porphyritic (299 Ma, Tochka, sample 7-236) granitoids were obtained previously (Kuibida et al., 2009).

The granite porphyry of the Kunush dyke was studied to determine the age of the high-Na dyke series. Zircon grains of 7-694 isolated for LA-SF-ICP-MS U–Pb dating are transparent colorless or pale yellow euhedral prismatic crystals (120-200 μm, K_L = 2.0–4.0, up to 6.0-7.0 in some cases), with a clear oscillatory magmatic zoning in CL images (Fig. 3e). The $^{206}Pb/^{238}U$ ratios give a concordant age of 305±2 Ma (MSWD = 0.1) (Fig. 4e), based on 17 analyses (Nos. 122-151, Table 1). CL images also show the presence of relict xenogenic

zircons which belong to several $^{206}Pb/^{238}U$ age groups: 344–332 Ma, 405–365 Ma, ~520 Ma, 925–847 Ma and ~1173 Ma (Nos 139-151 in Table 1). Two former age groups are widespread among igneous rocks of the Altaids (e.g. Wang et al., 2009), and two latter ones are typical of zircons from high-grade metamorphic rocks in the Irtysh-Zaisan orogen (Yermolov, 2013).

The porphyritic granite of the Besterek intrusion was previously considered to be coeval to the Kunush, Tochka, Zhilandy and other granitoids of the Kunush intrusive complex. Zircon grains of K-14-104 isolated for LA-SF-ICP-MS U–Pb dating are euhedral prismatic crystals (100–250 μm, K_L = 2.5–4.0), transluscent, colorless or pale yellow. CL images reveal thin oscillatory magmatic zoning and scarce relict xenogenic zircons (Fig. 3g). The $^{206}Pb/^{238}U$ age for these points (Fig. 4g) based on 22 analyses (Nos. 152-173, Table 1) corresponds to a concordant value of 292±2 Ma (MSWD = 0.01).

4.2. Petrography and mineralogy

4.2.1. Kunush intrusive complex

Massive granites were studied in the Zhilandy intrusion. The rocks consist of plagioclase of two generations (55 %), quartz (28–35%), biotite (5–10%), and minor amounts of K-feldspar (Fig. 5a). Zonal and polysynthetic plagioclases occur as euhedral long-prismatic (An_{30-44}, 30%) and subhedral short-prismatic grains (An_{25}, 25%). Quartz is generally anhedral and shows cloud extinction while biotite has undergone plastic deformation and displays subparallel orientation. The porphyritic granites were studied in the Tochka and Besterek intrusions. They are macroscopically different from their equigranular counterparts because of grain sizes but have similar mineralogy under the microscope (Fig. 5b, c). Porphyritic structure shows up most clearly in cataclastic varieties in which the intergranular space around quartz phenocrysts in the quartz aggregate displays cloud extinction. Plagioclase of two generations occurs as euhedral short-prismatic zoned grains (An_{25-32}) which form aggregates in the rock matrix. Some varieties enclose xenogenic garnet, clinopyroxene,

corundum, and kyanite. Surprisingly, the porphyritic granite of the Besterek intrusion shares petrographic and mineralogical similarity with other porphyritic granites of the Kunush complex in the region but it has experienced no shearing and has a younger age (it may have emplaced in the end of the magmatic cycle). The granite porphyry of dykes near the Zhilandy, Tochka and Kunush intrusions are composed of zoned platy plagioclase phenocrysts (An_{35-40}, 25–30%) in a matrix of fine-grained plagioclase (An_{25-30}, 20–25%), subhedral quartz (30%), ductily deformed biotite (10–15%) and minor K-feldspar (3–5%), with a mylonitic and blastomylonitic structure (Fig. 5d). Accessories are apatite, zircon, and titanite in all rocks; magnetite and amphibole are very rare.

4.2.2. Kalguty intrusive complex

The Kalguty rocks are of early, late, and final phases distinguished on the basis of lithology and intrusion order. The early phase (Kurchum intrusion) is coarse- to fine-grained gray quartz-monzonite consisting of euhedral long-prismatic zoned grains of andesine-oligoclase phenocrysts (An_{18-25}, 35 %), quartz (20%), K-feldspar (35–40%) and biotite (10–15%) (Fig. 5e), as well as xenogenic clinopyroxene, andalusite and pyrope-almandine garnet (18–25% of pyrope). The late phase (Kurchum intrusion) is coarse-grained gray quartz-monzonite, with a mineralogy consisting of plagioclase (40–50%), K-feldspar (25–30%), quartz (20%), and biotite (10–15%). The plagioclases are of several generations existing as porphyritic subhedral short-prismatic zoned grains (An_{48-50} and An_{35-40}) and as a matrix mineral (An_{18-30}) (Fig. 5g). Granites contain xenogenic pyroxenes. The final monzogranite phase (Kurchum intrusion) consists of plagioclase (35%), K-feldspar (33%), quartz (20–25%), biotite (5%), and amphibole pseudomorphs after clino- and orthopyroxene. The granodiorite of the Razdolny intrusion has been traditionally considered as an age equivalent of the Kurchum intrusion granitoids on the basis of mineral, petrographic, and chemical similarity (Lopatnikov et al., 1982; D'yachkov et al., 1994; Shcherba et al., 1998, etc.). This

interpretation is consistent with our microscopy data (Fig. 5f) but, on the other hand, the Razdolny granodiorite shows younger $^{206}Pb/^{238}U$ ages (see Section 4.1). Quartz-monzonite porphyry and porphyritic quartz-monzonite were studied in the VDN-dyke. They are composed of plagioclase phenocrysts (An_{35-40}, 30–35%), quartz (20%), K-feldspar (25-30%) and biotite (10–15%) (Fig. 5h). Accessories are apatite, zircon, and titanite in all rocks; magnetite and amphibole are very rare.

In addition to the unusual mineralogy with corundum, hedenbergite, andalusite, labrador, and pyrope-almandine garnet, the Kalguty plutonic rocks contain abundant crustal xenoliths consisting of biotite, biotite-garnet and biotite-sillimanite gneisses, and the late phase encloses feldspar-pyroxene-amphibole (granulite) xenoliths (Lopatnikov et al., 1982).

4.3. Major- and trace-element chemistry

4.3.1. Kunush intrusive complex

Representative analyses of major and trace elements (in wt.% and ppm) in the high-Na granitoids are listed in Table 2 (for analytical details see section 3). Most of modal compositions plot in the fields of tonalite and trondhjemite, in the An-Or-Ab triangle diagram (Fig. 6a; O'Connor, 1965; Barker, 1979). The rocks contain 67–72% SiO_2 and 15–18% Al_2O_3 and have low K_2O/Na_2O (0.12–0.66) and high Sr/Y (47–179) ratios. Chondrite-normalized REE patterns (C1 chondrite values of Sun and McDonough, 1989; Fig. 7a, b) are moderately differentiated with $(La/Yb)_n$ = 8-26 and low HREE (Yb = 0.22–0.93 ppm). These rocks can be attributed to the high-Al tonalite-trondhjemite-granodiorite (TTG) series (Arth, 1979), based on their Al_2O_3 content (>15 wt.%) at 70 wt.% SiO_2, a high Sr/Y ratio of >40, and low Yb (< 1.8 ppm). The Kunush granitoids have Mg-numbers (*Mg#*) = 35-55 (n=55; database of Lopatnikov et al. (1982) and *Mg#* = 57-62 (n=7) at SiO_2 = 67–72 wt.%. These values are also typical of TTG-series with *Mg#* = 41–53 (Smithies, 2000) rather than Cenozoic HAS (high-Si adakite with >60 wt.% SiO_2 and average *Mg#* = 48–64 (Martin et al., 2005)). The Mg

numbers (%) were calculated as the molecular ratio of Mg/(Mg+Fe^{2+}), where Fe^{2+} is assumed to be 90% of total iron. The Kunush granitoids have Sr (418–727 ppm) values are also common to TTG (Sr = 362–596 ppm) but different from the HSA values (Sr = 706–2366 ppm); (Smithies, 2000). Their Nb/Ta ratios are lower than in adakites (3-16 against 15-20) but approach those of primitive mantle (16.7), while the Zr/Sm ratios are greater than the PM values (37.9-79.5 against 25.2, respectively). The sum Na_2O+CaO (7.3–9.7 wt.%) is lower than in HSA (Condie, 2005), and the Cr (6.5-39.4 ppm) and Ni (10.9-26.8 ppm) contents at 67–72% SiO_2 are inconsistent with slab-derived adakite signatures (Wang et al., 2006).

The multi-element normalized patterns (McDonough et al., 1992) of intrusive rocks from different phases are generally similar and parallel, with slight to moderate variations in element abundances. Massive and porphyritic granitoids differ from those with other structure types, especially in higher Sr, but there are also transitional varieties. Granite porphyry differs from other types in lower contents of Sr and CaO with significant enrichment in LREE, Th, Hf, Ta and Zr. The multi-element patterns of the Kunush high-Na granitoids show prominent negative Nb-Ta and positive Zr-Hf anomalies, which both are generally typical of supra-subduction and non-subduction settings (see the citations below). The rock compositions plot off the field of slab-derived adakite in the Ca-Na-Mg diagram (Fig. 6b) but rather fall within the field of lower crust-derived high-Na granitoids from Andean-type overthickened orogens and post-orogenic extension settings (Muir et al., 1995; Petford and Atherton, 1996; Johnson et al., 1997; Xiong et al., 2003; Chung et al., 2003; Karsli et al., 2011).

4.3.2. Kalguty intrusive complex

Representative analyses of major and trace elements (in wt.% and ppm) in high-K granitoids are listed in Table 3. They show moderate contents of SiO_2 (62.2–74.2 wt.%) at high Na_2O (3.1–4.6 wt.%) and K_2O (2.1–5.3). The Kurchum and VDN-dyke granitoids, with K_2O+Na_2O = 6.7–9.1 wt.%, plot within the subalkaline field in the TAS diagram (Le Maitre,

1989) (Fig. 8a) and within high-K calc-alkalic compositions in the SiO_2-K_2O diagram (Peccerillo and Taylor, 1976); Fig. 8b. The K_2O-rich chemistry of quartz-monzonite (3.0-4.6 wt.%) and monzogranite (3.8–5.3 wt.%) shows up in mineralogy as abundant alkali feldspar and biotite, which is consistent with positive K-feldspar-to-plagioclase correlation ratios (K_2O/Na_2O = 0.8–1.6). In contrast, the rock compositions of the Razdolny intrusion fall in the field of granodiorite but overlap with quartz-monzonite and correspond to the high-K calc-alkalic series (K_2O/Na_2O = 0.5–1.3; K_2O+Na_2O = 6.2–7.3; K_2O = 2.1–4.2 wt. %).

Most granitoids show non-corundum CIPW-norm compositions (*C* = 0.16–0.96, n = 35), except for the perfectly corundum-normative (*C* = 1.6–2.5) VDN-dyke and some corundum-normative samples within each group of rocks (*C* = 1.2–2.4, n = 9). According to the Aluminium Saturation Index (Zen, 1986) used to discriminate between *I*-type (*ASI* < 1.1) and *S*-type granites (*ASI* > 1.1), the compositions are mainly weakly peraluminous (0.97–1.09, n = 32) and few are strongly peraluminous (1.1-1.19, n = 13); (Fig. 8c). In the SiO_2-*Fe** diagram (Fig. 8d) discriminating between ferroan and magnesian series (Frost et al., 2001), quartz-monzonite and granodiorite fit the boundary between the two (*Fe** = 0.7–0.8 at SiO_2 = 62-68 wt.%), while monzogranite plots within the ferroan field, with *Fe** = 0.8–1.0 at SiO_2 = 72-74 wt.% (*Fe** = $FeO^{tot}/(FeO^{tot} + MgO)$). As the rocks become more felsic, they generally increase in Al_2O_3, K_2O and *Fe** enrichment and show negative correlation with P_2O_5, which is common to *I*-type granites (Chappell and White, 1992; Chappell, 1998).

The incompatible Rb/Sr ratios (0.4–1.0) of quartz-monzonite and granodiorite (exclusive of monzogranite) also have typical *I*-granite ranges corresponding to high Sr and low Rb (Whalen et al., 1987). The HFSE (Th, Nb, Y) and LREE contents are in the normal range but their sum exceeds that in *M*-, *I*- and *S*-granites because of high Zr (140–386 ppm) (Chappell, 1999; Fig. 9a). The quartz-monzonite and granodiorite, with 62.2–69.5 wt.% SiO_2, Na_2O+K_2O = 6–9 %, and CaO > 1.8% (1.8-3.8 wt.%), differ from FG-type (fractionated *I*-type granite; Fig. 9a) but their Y/Nb (2–4) and Rb/Nb (9–18) ratios are similar to those in

some of *A*-type granites worldwide (Fig. 9b, c; Collins et al., 1982; Whalen et al., 1987; Eby, 1992). In contrast, the monzogranite samples show signatures similar to FG-type (Chappell, 1999): low CaO (0.8-1.5 wt.%), high K_2O (3.84–5.33 wt.%), predominantly weakly peraluminous compositions (*ASI* = 1.0–1.1), very low Sr (37–48 ppm; Rb/Sr = 4.7–5.3) and Ba (89–160 ppm; Rb/Ba = 1.4–2.2), and high *Fe** (0.8–1.0), except for two samples (Fig. 8d; Table 3). In the Nb vs. Y and Rb vs. Y+Nb tectonic discrimination diagrams (Pearce et al., 1984), the granitoid compositions plot within the post-collisional A_2-type field (Fig. 9b, c; Whalen et al., 1987). The content of Zr and Hf of the Kalguty granitoids vary coherently as a function of Fe+Mg and decrease at increasing Na+K and SiO_2, similar to the behavior of the high-temperature *I*-type felsic magmas (King et al., 2001; Fig. 9d).

The LREE and HREE patterns in quartz-monzonite and granodiorite are similar (La = 21–50 ppm and Yb = 2.1–3.5 ppm). The rocks show similar slightly fractionated patterns in chondrite-normalized diagrams (C1 chondrite values of Sun and McDonough, 1989), with LREE over HREE enrichment (La/Yb_N ratios of 4-13; ΣREE = 151–224 ppm), and a moderate negative Eu anomaly (Eu/Eu* = 0.4–0.6; Fig. 7c). The PM-normalized element patterns are also homogeneous with prominent and uniform negative anomalies in Ba, Nb, Ta, Sr, and Eu, and with slight to moderate variations in element abundances. The REE patterns of monzogranites contain less LREE and more HREE, which produces flat REE spectra (La/Yb_N ratios of 3-7). Along with a large negative Eu anomaly (Eu/Eu*~0.1), these spectra resemble the sigmoidal patterns of some *A*-type granites (Fig. 7c). The PM-normalized patterns also show prominent negative Ba, Sr anomalies and elevated Rb and Zr.

In general the obtained REE patterns correspond to transitional compositions reported for the fractionated *I*-granite and A_2-granite which may be attributed to post-orogenic lithospheric extension (Chappell and White, 1992; King et al., 1997; Chappell, 1999).

5. Discussion

5.1. Petrogenesis of the Kunush high-Na granitoids

TTG rocks, possibly, ancient analogs of Phanerozoic granitoids, were produced in a subduction-accretionary setting, by melting of subducted slabs (dehydrated MORB and/or eclogite) and/or accreted basaltic oceanic crust and oceanic plateaus containing recycled crustal material eroded from adjacent arcs at lower crust depths (Berd and Lofgan, 1991; Rapp and Watson, 1995; Winther, 1996; White et al., 1999; Smithies, 2000; Rapp et al., 2003; Chung et al., 2003). In the latter case, many studies interpreted "slab-like" melts as being derived from overthickened hydrous juvenile lower crustal (amphibolitic) protoliths under garnet-stable *P–T* conditions (e.g., Barnes et al., 1996; Petford and Atherton,1996; Johnson et al.,1997; Whalen et al., 2002; Chung et al., 2003; Turkina, 2005; Karsli et al., 2011). One possible mechanism for the adakite-like magma generation in overthickened orogens is thermal relaxation and decompression leading to partial melting early during exhumation of continental crust at ultrahigh pressures (Song et al., 2014). Another mechanism is delamination of the continental lithosphere, asthenospheric upwelling and thermal impact of mafic magma on the lower/middle crust (Elkins-Tanton, 2005).

Most of the geological facts discussed above indicate that the Kunush high-Na granitoids apparently originated in a non-subduction setting, as a result of partial melting of the thickened mafic lower crust in the Kalba fold belt. There are several lines of evidence in support of this inference.

First, the Kunush high-Na granitoids display positive $\varepsilon Nd_{(300\ Ma)}$ from 6.7 to 8.9 isotopic values and T_{DM} ages (351-532 Ma) indicating that their parent magma resulted from partial melting of a source containing relatively younger (juvenile) mantle-derived component and are consistent with their TTG nature. The Sm-Nd isotopic characteristics suggest that the protolith of the high-Na granitoids is similar to metabasalts (rutile-titanite-bearing eclogites, blueschists, and amphibolites) found along the Chara ophiolite zone and Irtysh shear zone, with $\varepsilon Nd_{(300\ Ma)}$ from +3.5 to +9.8 (Hu et al., 2000; Volkova and Sklyarov, 2007; Safonova et al., 2012; Kuibida et al., 2012; Kotler et al., 2015; Safonova et al., 2018); Fig. 10. Some of

these oceanic basalts were exhumed in the Late Ordovician (~450 Ma; Volkova et al., 2008) and make up the main volume in the lithology of the Chara ophiolite zone; others have been generated during the Early Carboniferous evolution of the Kalba fold belt (~350 Ma; Safonova et al., 2012). The Kunush high-Na granitoids may have been derived from different metabasalts of accreted oceanic crust that underlie the metamorphic lithology of the Kalba fold belt, rather than from a homogeneous oceanic slab.

Second, the trace element patterns of the high-Na granitoids indicate that their source had Nb/Ta ratios (3-16) lower than in chondrite and low Zr (Fig. 11a), which are commensurate with the values inferred for Chara amphibolites with Nb/Ta = 8-17 and Zr = 1-72 ppm (Volkova et al., 2008). In addition, fragments of mafic to felsic volcanic and subvolcanic rocks in ophiolitic melange (Yermolov, 2013) possess geochemical signatures of island-arc series (Volkova et al., 2008; Safonova et al., 2018) and hence may have been involved into magma generation.

Third, experimental modeling of partial melting for a mafic source shows that high-Al and low-HREE (Yb < 0.8 ppm) sodic felsic melts can form in equilibrium with garnet-bearing residual assemblages (Wolf and Wyllie, 1994; Sen and Dunn, 1994; Rapp and Watson, 1995). The dehydration melting of amphibolitic protoliths that can leave garnet residue requires at least ≥12 kbar (35 km), while the eclogitic residue forms at higher pressures (>20 kbar or >70 km). Low Nb/Ta ratios (3-16) in the Kunush high-Na granitoids suggest the presence of rutile in the residual assemblage and the same low ratios in molten rutile, in which Nb and Ta are compatible at P < 15 kbar (Foley et al., 2000; Barth et al., 2002; Xiong et al., 2005). However, low concentrations of Nb (0.99-2.74 ppm) and Ta (0.08-0.27 ppm) rather correspond to intermediate or great generation depths of the Kunush parent melts (Moyen and Martin, 2012); Fig. 11b. Two high-Na granite porphyry samples with Nb = 6.6-7.5 ppm and Ta = 0.42-0.78 ppm may come from intermediate to shallow depths. The present 47±6 km crust thickness in the Kalba fold belt, as estimated by geophysical methods (Shcherba et al., 1998),

is consistent with the depth range from 27 km (Tate and Johnson, 2000) to >40 km (Petford and Atherton, 1996) for the generation of adakitic-like melts by partial melting of metabasaltic lower crust in an orogenic belt.

5.2. Petrogenesis of the Kalguty high-K granitoids

There are several key points necessary for understanding and reconstructing the petrogenesis of the Kalguty high-K granitoids. First, their isotope signatures indicate possible presence of mixed mantle and crustal components ($\varepsilon Nd_{(300\ Ma)}$ from 2.1 to 3.5; Table 4; Fig. 10). The formation of *I*-type granites (e.g. monzogranite) with hybrid mantle-crustal isotope ratios was often attributed to interactions of metamorphic crust with hot alkaline magmas. The process was suggested to involve metasomatism of the lithospheric mantle and mixing or mingling of mafic magmas with felsic melts (see criticism by Clemens et al., 2011; Clemens and Stevens, 2012). However, mantle-crust interactions hardly could be a major process in generation of the Kalguty parental magma, for several reasons. (i) The preserved rock record lacks dark microgranular enclaves. (ii) The granitoids fail to show pairwise correlations of major oxides in the Harker plots diagnostic of mixing between end-members of two contrast melts (Chappell, 1996). (iii) Neither two-component mixing nor reactions of basalts and metamorphic rocks produced high-K calc-alkaline felsic melts in experiments on dehydration melting (Johnstone and Wyllie, 1988; Carroll and Wyllie, 1989; Douse, 1995; Castro et al., 1999; Lopez et al., 2005). The granite of this type also might have formed by fluid-absent partial melting of previously accreted crust heated by underplated mafic magma (Robert and Clemens, 1993). However, the experimental evidence suggests that melts originate from a mechanically mixed heterogeneous source having a bulk tonalitic to granodioritic composition (Skjerlie et al., 1993; Skjerlie and Douce, 1995; Castro et al., 2010).

Second, various crustal xenoliths and xenocrysts captured by granitic magma are amphibolite- and granulite-facies rocks metamorphosed under pressures of 4 to 12 kbar

(Pattison et al., 2003). If the high-grade metamorphic crust of the Kalba fold belt were a source for the Kalguty parental magma, the granitoids would be expected to originate at pressures and temperatures similar to those of metamorphism. However garnet hardly took part in the generation of the Kalguty parental magmas: otherwise one would expect more strongly peraluminous values common to the S-type granites (Stevens et al., 2007; Clemens et al., 2011), or adakitic signatures (Xiao and Clemmens, 2007). The exotic xenoliths and xenocrysts may have been captured by granitic magmas from a crustal source outside the garnet stability field in the course of fast exhumation of high-grade metamorphic crust.

Third, melting or assimilation of an ancient continental crust source, which would explain high Zr enrichment (Clemens et al., 1986; Eby, 1990), cannot be major factors in the generation of granitoids with positive εNd(t) values, for the lack of inherited zircon crystals (see Section 4.1.1). The Zr enrichment (140-386 ppm) of the Kalguty granitoids may be due to rapid dissolution of accessory zircon during water-saturated melting (amphibolite facies) whereby melts gain heat-producing and incompatible elements (U, Th, Zr, LREE) (Watson and Harrison, 1983; Rapp and Watson, 1986). The behavior of zircon in the Kalguty granitoids (see Zr vs. SiO_2 variation diagrams in Fig. 9d) with the greatest abundance of most mafic varieties (less than ~68% SiO_2) and the decrease towards more felsic compositions, is similar to the trends in *A*- and *I*-types granites derived from a quartz-feldspathic source at Zr-saturated crystallization (King et al., 2001).

There are two main candidates for the source of the Kalguty high-K granitoids. (i) Metasediments originated from supra-subduction volcanic rocks and granitoids, with $\varepsilon Nd_{(300\ Ma)}$ from +0.7 to +4.4 and model age (T_{DM}) between 0.85 and 1.61 Ga (our data), which were possibly transported from the Altai active margin to the Kalba fore-arc basin. The high-K metaluminous to weakly peraluminous granites can be produced by melting of volcanoclastic rocks derived from a high-K andesitic/dacitic arc source (Clemens et al., 2011). In this case, the isotopic system of immature sediments (deposited shortly before being partially molten) is

expected to keep record of the mantle link in the granitic magma. (ii) Metaigneous rocks from the Kalba high-grade metamorphic lithology (Yermolov, 2013) similar to basement granitic gneisses in the adjacent territory of Chinese Altai, with $\varepsilon Nd_{(300\ Ma)}$ from +1.8 to +3.2 and T_{DM} ages between 0.89 and 0.96 Ga (Hu et al., 2000; Briggs et al., 2007); Fig. 10. The granites of this type could be formed by partial melting of a metaigneous tonalite/granodiorite protolith, as suggested by experimental studies (Skjerlie and Johnston, 1992; Singh and Johannes1996; Douse, 1997). Moreover, the crust over a large part of the Kalba fold belt includes a 5-14 km thick middle layer of metadiorite below the 14-18 km depth, which is composed mainly of garnet-sillimanite-two-mica granitic gneiss, migmatites and paragneiss containing quartz-feldspar-biotite and feldspar-amphibole-clinopyroxene assemblages (Shcherba et al., 1998; Plotnikov et al., 2003; Yermolov, 2013).

We checked the hypothesis by identifying crustal sources and comparing the compositions of the Kalguty high-K granitoids with those obtained in melting experiments for metasedimentary-, metaigneous-, volcanic- and mechanically mixed-sources, using the exclusion approach. In the comparison, two limiting criteria were taken into account: (i) the garnet stability field is from 4 kbar for metasedimentary sources (Vielzeuf and Montel 1992) and from 8–10 kbar for tonalite sources (Rutter and Wyllie 1988; Watkins et al., 2007). (ii) The melt fraction that allows segregation and ascent of granitic melts from their sources is bracketed between 20% and 60% (Vanderhaeghe, 2009). In general, the Kalguty granitoids are compositionally similar to the experimental melts derived from diorite and biotite-rich tonalities (Skjerlie and Johnston, 1992; Singh and Johannes1996; Douse, 1997), and their protolith is more likely of metaigneous rather than metasedimentary or hybrid origin (Fig. 12).

5.3. Tectonic implications

5.3.1. Review of the pre-collision stage

According to some viewpoints the convergence of the Irtysh-Zaisan oceanic plate and the Siberian continent continued until the Late Carboniferous-Early Permian (e.g. Li et al., 2017; Chen et al., 2017; Safonova et al., 2018b). Our alternative conceptual scenario (see the schematic cartoon in Fig. 13) presents the Late Paleozoic geodynamic evolution of the Irtysh-Zaisan orogen based on peaks of magmatic activity, with reference published results for the adjacent territory of CAOB (see the citations below). However, the tectonic settings are reconstructed proceeding not only from major- and trace-elements compositions and isotope systematic of magmatism. Reliable paleotectonic reconstructions require due regard for regional geology, types of magmatic associations, sedimentation and deformation. Note especially that the formation of granitoids within oceanic plates rules out subduction, except for the specific case of "ophiolite plagiogranites".

We hypothesize that the continental margin transform motions occurred along the Altai margin of Siberia from the Late Devonian to the latest Early Carboniferous. Firstly, the formation of an accretionary wedge of the Kalba fore-arc belt in front of the Altai active margin stopped at the Eifelian-Jivetian boundary (Scherba et al., 1998). Second, it was accompanied by shearing and thrusting of the margin terranes, HT\LP metamorphism, and generation of accretionary granitoids (Alaskan-type) at 362-352 Ma (Kuibida et al., 2012; Yermolov, 2013). Third, the activity was followed by transtension (Scherba et al., 1998) and the formation of dolerite and andesite dykes and granite linear intrusions along the Altai continental margin at 340-333 Ma (Vladimirov et al., 2001). Before this period, volcanism in the Zharma-Saur active margin marked, probably, the final stage of convergence between the Irtysh-Zaisan oceanic and Kazakhstan continental plates at 347-343 Ma (Shen et al., 2008).

5.3.2. Review of the syn- and post-collision stages

The collisional stage (end-Early Carboniferous) is indicated by deposition of the Serpukhovian conglomerates that overlie the Visean serpentinite mélange of the Chara

ophiolite zone (Yermolov et al., 1981; Scherba et al., 1998). Non-subduction lower crust-derived granitoids (TTG-type) formed under the effect of faulting at 75º and 310º at 324-318 Ma (Kuibida et al., 2013) on the Altai continental margin, as well as within the oceanic plate in the Chara suture zone between Siberia and Kazakhstan at 323 Ma (Yermolov et al., 1983; Kuibida et al., 2016); Fig. 13a. We suggest that it was somehow related with the intrusion of gabbro (321 Ma; Deng et al., 2017) and high-*Mg#* dioritic dykes controlled by a system of 280-310º faults (321 Ma; Yin et al., 2010) in the Junggar plate and with tonalite magmatism in SW Chinese Altai at 318 Ma (Yuan et al., 2007). The synchronous formation of molasse (from Serpukhovian to Moscovian) and non-subduction granitoids derived from the lower crust within the oceanic plate is the key evidence of the Late Carboniferous crustal thickening in the Irtysh-Zaisan tectonic belt, in the absence of subduction.

Numerous examples of high-temperature granite magmatism in post-orogenic settings, with Late Carboniferous – Early Permian zircon U–Pb ages between 320 and 265 Ma, have been reported from many parts of CAOB: Junggar, Chinese Altai, Tian-Shan and Eastern Kazakhstan (Han et al., 1997; Cai et al., 2001; Chen and Jahn, 2004; Vladimirov et al., 2008; Wang et al., 2009; Chen et al., 2010; Han et al., 2010; Yuan et al., 2010; Yang et al., 2011; Chen et al., 2011; Shen et al., 2011; Gao et al., 2014; Zhang et al., 2015; Kotler et al., 2015; Khromykh et al., 2016; Zhao et al., 2016; Yuan et al., 2016; Liu et al., 2017). The cited models predict a change of setting from compression to extension after the collision, which led to removal of lower subcontinental lithospheric mantle and the following extensional collapse of the orogen, upwelling of asthenospheric mantle, and generation of basaltic and voluminous high-temperature *A*-type granitic magmas with subordinate amounts of calc-alkaline magmas.

In the Kalba fold belt gabbro record the onset post-collisional activity at 317-312 Ma (Khromykh et al., 2016, 2018), with later generation of the Kunush high-Na and Kalguty high-K granitoids at 308-291 Ma (Fig. 13b). The subsequent formation of gabbro and picrites

(Zhang et al., 2012; Khromykh et al., 2013), as well as the giant Kalba-Narym granitoid batholith, at 296-276 Ma (Kotler et al., 2015; Khromykh et al., 2016) corresponds to maximum extension, when a large portion of crust (lower to middle) was involved into partial melting. The Early Permian evolution of the Kalba fold belt can be explained with a model of a "hot shear system" (Vladimirov et al., 2008). The extremely voluminous magmatism was an aftereffect of the oblique collision of Kazakhstan and Siberia and their post-collisional interaction during continuing rotation of the two continental plates relative to one another. Probably, the relaxation of tangential compression and the thermal-mechanical impact of mafic magma on the lower/middle crust, along with decompressional partial melting of metamorphic lithology, may be the basic petrological scenario.

In general, we infer that the Late Paleozoic Irtysh-Zaisan orogen evolved in a setting of oblique interaction between oceanic and continental plates, with rhythms of transpression and shear to maximum compression (collision stage) in the end-Early Carboniferous, and the following maximum extension (post-collision collapse) in the Late Carboniferous – Early Permian. The question is to choose between the "passive" and "active" mantle models of voluminous asthenospheric upwelling or a superplume, respectively, to explain the Late Carboniferous–Early Permian tectonic-thermal evolution in the Central Asian Orogenic Belt.

6. **Conclusions**

The reported field data from the Irtysh-Zaisan orogen (Eastern Kazakhstan), zircon U–Pb dates, Nd–isotope systematics, as well as whole-rock major- and trace-element compositions, supported by published evidence on the Late Carboniferous – Early Permian magmatism from the surrounding areas, allow the following inferences.

(1) The Kunush high-Na and Kalguty high-K contrasting granitoids emplaced synchronously between 308 and 291 Ma into the thick crust of the Kalba fold belt in front of

the Altai margin of Siberia. The granitoids show divergent geochemical signatures related to felsic magmatism in an overthickened orogen and a post-orogenic extension setting.

(2) The Kunush and Kalguty granitoids formed by decompressional partial melting at different depths in the crust. The parent melts of the high-Na and high-K granitoids were derived from metabasaltic (MORB; P = 10-15 kbar) and metagranitic (TTG; P < 10 kbar) protoliths, respectively. The relaxation of tangential compression and horizontal motion along the suture between Siberia and Kazakhstan during their rotation relative to one another may have caused asthenospheric upwelling and the onset of widespread crustal melting, according to the "hot shear system" model.

(3) In general, the Late Carboniferous – Early Permian large-scale melting is recorded in a series (magmatic column) of chemically different granitoids from the Kunush high-Na and Kalguty high-K granitoids to the Kalba-Narym C- and A_2-type granitoids at 308- 276 Ma, which were generated coevally with the post-orogenic magmatic peak at ~300 Ma in the Altaids.

Acknowledgments

We dedicate this paper to the memory of the late Oleg V. Navozov, a prominent geologist, who spent more than fifty years studying granitic rocks in Eastern Kazakhstan.

The study was carried out as part of a basic research program at the V.S. Sobolev Institute of Geology and Mineralogy (Project No. 0330-2016-0003) and was additionally supported by the Ministry of Science and Education of the Russian Federation (Projects Nos. 14.Y26.31.0018 and 5.1688.2017/PCh). We greatly appreciate fruitful and encouraging discussions with Olga Turkina, Andrei Izokh, Vladimir Vladimirov and Inna Safonova, as well as collaboration in the field with Kazakhtan geologists. Writing this paper would be impossible without years of the hard field and laboratory work of skillful geologists from

Russia, China and Kazakhstan and analytical support by N.G. Karmanova, I.V. Nikolaeva (IGM SB RAS, Novosibirsk) and V. B. Khubanov (IG SB RAS, Ulan-Ude).

References

Alonso–Perez, R., Muntener, O., Ulmer, P., 2009. Igneous garnet and amphibole fractionation in the roots of island arcs: experimental constraints on andesitic liquids. Contributions to Mineralogy and Petrology 157, 541–558.

Arth, J.G., 1979. Some trace elements in trondhjemites - their implications to magma genesis and paleotectonic setting. In: Barker, F. (Ed.), Trondhjemites, Dacites, and Related Rocks. Elsevier, Amsterdam, pp. 123–132.

Barker, F., 1979. Trondhjemites: definition, environment and hypotheses of origin. In: Barker, F. (Ed.), Trondhjemites, Dacites and Related Rocks. Elsevier, Amsterdam, pp. 1–12.

Barnes, C., Petersen, S., Kistler, R., Murray, R., Kays, M., 1996. Source and tectonic implication of tonalite-trondhjemite magmatism in the Klamath Mountains. Contributions to Mineralogy and Petrology 123, 40–60.

Barth, M.G., Foley, S.F., Horn, I., 2002. Partial melting in Archean subduction zones: constraints from experimentally determined trace element partition coefficients between eclogitic minerals and tonalitic melts under upper mantle conditions. Precambrian Research 113, 323–340.

Beard J.S., Lofgren, G.E., 1991. Dehydration melting and water-saturated melting of basaltic and andesitic greenstones and amphibolites at 1, 3, and 6.9 kb. Journal of Petrology 32, 365–401.

Black, R., Liégeois, J.P., 1993. Cratons, mobile belts, alkaline rocks and continental lithospheric mantle: the Pan-African testimony. Journal of the Geological Society 150, 89–98.

Briggs, S.M., Yin, A., Manning, C.E., Chen, Z.L., Wang, X.F., Grove, M., 2007. Late Paleozoic tectonic history of the Ertix Fault in the Chinese Altai and its implications for the development of the Central Asian Orogenic System. Geological Society of America Bulletin 119, 944–960.

Buslov, M.M., Saphonova, I. Yu, Watanabe, T., Obut, O.T., Fujiwara, Y., Iwata, K., Semakov, N.N., Sugai, Y., Smirnova, L.V., Kazansky, A.Yu, Itaya, T., 2001. Evolution of the Paleo-Asian Ocean (Altai-Sayan, Central Asia) and collision of possible Gondwana-derived terranes with the southern marginal part of the Siberian continent. Geoscience Journal 5, 203–224.

Buslov, M.M., Watanabe, T., Fujiwara, Y., Iwata, K., Smirnova, L.V., Safonova, I. Yu, Semakov, N.N., Kiryanova, A.P., 2004. Late Paleozoic faults of the Altai region, Central Asia: tectonic pattern and model of formation. Journal of Asian Earth Sciences 23, 655–671.

Cai, K., Sun, M., Yuan, C., Zhao, G., Xiao, W., Long, X., Wu, F., 2011. Prolonged magmatism, juvenile nature and tectonic evolution of the Chinese Altai, NW China: evidence from zircon U–Pb and Hf isotopic study of Paleozoic granitoids. Journal of Asian Earth Sciences 42, 949–968.

Carroll, M.R., Wyllie, P. J., 1989. Experimental phase relations in the system tonalite-peridotite-H_2O at 15 kb; implications for assimilation and differentiation processes near the crust-mantle boundary. Journal of Petrology 30, 1351–1382.

Castro, A., Patiño Douce, Corretgé, L.G., Jesús, D., El-Biad, M., El-Hmidi, H., 1999. Origin of peraluminous granites and granodiorites, Iberian massif, Spain: an experimental test of granite petrogenesis. Contributions to Mineralogy and Petrology 135, 255–276.

Castro, A., Gerya, T., Garcна-Casco, A., Fernбndez, C., Dнaz-Alvarado, J., Moreno-Ventas, I., Lцw, I., 2010. Melting relations of MORB–sediment mйlanges in underplated mantle

wedge plumes; implications for the origin of Cordilleran-type batholiths. Journal of Petrology 51, 1267–1295.

Chappell, B.W., 1979. Granites as images of their source rocks. Geological Society of America, Abstract Progr. 11, 400.

Chappell, B.W., White, A.J.R., 1992. I-and S-type granites in the Lachlan Fold Belt. Geological Society of America Special Papers 272, 1–26.

Chappell, B.W., 1996. Magma mixing and the production of compositional variation within granite suites: evidence from the granites of southeastern Australia. Journal of Petrology 37, 449–470.

Chappell, B.W., Bryant, C.J., Wyborn, D., White, A.J.R., Williams, I.S., 1998. High-and Low-Temperature I-type Granites. Resource Geology 48, 225–235.

Chappell, B.W., 1999. Aluminum saturation in I-and S-type granites and the characterization of fractionated haplogranites. Lithos 46, 535–551.

Chen, B., Jahn, B.M., 2004. Genesis of post-collisional granitoids and basement nature of the Junggar Terrane, NW China: Nd–Sr isotope and trace element evidence. Journal of Asian Earth Sciences 23, 691–703.

Chen, J.F., Han, B.F., Ji, J.Q., Zhang, L., Xu, Z., He, G.Q., Wang, T., 2010. Zircon U–Pb ages and tectonic implications of Paleozoic plutons in northern West Junggar, North Xinjiang, China. Lithos 115, 137–152.

Chen, X., Shu, L., Santosh, M., 2011. Late Paleozoic post-collisional magmatism in the Eastern Tianshan Belt, Northwest China: new insights from geochemistry, geochronology and petrology of bimodal volcanic rocks. Lithos 127, 581–598.

Chen, Y., Xiao, X., Windley, B.F., Zhang, J., Zhou, K., 2017. Late Devonian-early Permian subduction-accretion of the Zharma-Saur oceanic arc, West Junggar (NW China): Insights from field geology, geochemistry and geochronology. Journal of Asian Earth Sciences 145, 424–445.

Chung, S.L., Liu, D., Ji, J., Chu, M.F., Lee, H.Y., Wen, D.J., Zhang, Q, 2003. Adakites from continental collision zones: melting of thickened lower crust beneath southern Tibet. Geology 31, 1021–1024.

Clemens, J.D., Holloway, J.R., White A.J., 1986. Origin of an A-type granite: experimental constraints. American Mineralogist 71, 317–324.

Clemens, J.D., Stevens, G., Farina, F., 2011. The enigmatic sources of I-type granites: the peritectic connexion. Lithos 126, 174–181.

Clemens, J.D., Stevens, G., 2012. What controls chemical variation in granitic magmas? Lithos 134, 317–329.

Collins, W.J., Beams, S.D., White, A.J.R., Chappell, B.W., 1982. Nature and origin of A-type granites with particular reference to southeastern Australia. Contributions to mineralogy and petrology 80, 189–200.

Condie, K.C., 2005. TTGs and adakites: are they both slab melts? Lithos 80, 33–44.

Conrad, W.K., Nicholls, I.A., Wall, V.J., 1988. Water-saturated and undersaturated melting of metaluminous and peraluminous crustal compositions at 10 kb: evidence for the origin of silicic magmas in the Taupo Volcanic Zone, New Zealand, and other occurrences. Journal of Petrology 29, 765–803.

Dyachkov, B.A., 1972. Intrusive magmatism and metallogeny of Eastern Kalba. Nedra, Moscow, 211 pp. (in Russian).

Dyachkov, B.A., Mayorova, N.P., Shcherba, G.N., Abdrakhmanov, K.A., 1994. Granitoid Suites and Ore Assemblages of the Kalba–Narym Belt (Rudny Altai). Gylym, Almaty (in Russian).

Davies, J.H., von Blanckenburg, F., 1995. Slab breakoff: a model of lithosphere detachment and its test in the magmatism and deformation of collisional orogens. Earth and Planetary Science Letters 129, 85–102.

Deng, Y.F., Yuan, F., Zhou, T., Hollings, P., Zhang, D., 2017. Geochemistry and tectonic implications of the Early Carboniferous Keketuobie intrusion in the West Junggar foldbelt, NW China. Journal of Asian Earth Sciences 159. DOI: 10.1016/j.jseaes.2017.09.014

Dawey, J.F., 1988. Extensional collaps of orogens. Tectonics 7, 1123–1139.

Dobretsov, N.L., Berzin, N.A., Buslov, M.M., 1995. Opening and tectonic evolution of the Paleo-Asian Ocean. International Geology Review 37, 335–360.

Douce, A.E.P., 1995. Experimental generation of hybrid silicic melts by reaction of high-Al basalt with metamorphic rocks. Journal of Geophysical Research: Solid Earth, 100 (B8), 15623–15639.

Douce, A.E.P., 1997. Generation of metaluminous A-type granites by low-pressure melting of calc-alkaline granitoids. Geology 25, 743–746.

Douce, A.E.P., 1999. What do experiments tell us about the relative contributions of crust and mantle to the origin of granitic magmas? Geological Society, London, Special Publications 168, 55–75.

Douce, A.E.P., Beard, J.S., 1995. Dehydration melting of biotite gneiss and quartz amphibolite from 3 to 15 kbar. Journal of Petrology 36, 707–738.

Douce, A.E.P., Beard, J.S., 1996. Effects of P, $f(O_2)$ and Mg/Fe ratio on dehydration melting of model metagreywackes. Journal of Petrology 37, 999–1024.

Eby, G.N., 1990. The A-type granitoids: a review of their occurrence and chemical characteristics and speculations on their petrogenesis. Lithos 26, 115–134.

Elkins-Tanton, L.T., 2005. Continental magmatism caused by lithospheric delamination. Geological Society of America Special Papers 388, 449–461.

England, P.C., Thompson, A., 1986. Some thermal and tectonic models for crustal melting in continental collision zones. Geological Society, London, Special Publications 19, 83–94.

Foley, S.F., Barth, M.G., Jenner, G.A., 2000. Rutile/melt partition coefficients for trace elements and assessment of the influence of rutile on the trace element characteristics of subduction zone magmas. Geochimica et Cosmochimica Acta 64, 933–938.

Frost, B.R., Barnes, C.G., Collins, W.J., Arculus, R.J., Ellis, D.J., Frost, C.D., 2001. A geochemical classification for granitic rocks. Journal of Petrology 42, 2033–2048.

Gao, R., Xiao, L., Pirajno, F., Wang, G.C., He, X.X., Yang, G., Yan, S.W., 2014. Carboniferous–Permian extensive magmatismin the West Junggar, Xinjiang, northwestern China: its geochemistry, geochronology, and petrogenesis. Lithos 204, 125–143.

García-Casco, A., Haissen, F., Castro, A., El-Hmidi, H., Torres-Roldán, R.L., Millán, G., 2003. Synthesis of staurolite in melting experiments of a natural metapelite: consequences for the phase relations in low-temperature pelitic migmatites. Journal of Petrology 44, 1727–1757.

Goldstein S.J., Jacobsen S.B., 1988. Nd and Sm isotopic systematics of rivers water suspended material: Implications for crustal evolution. Earth. Planet Sci. Lett. 87, 249–265.

Griffin W.L., Powell W.J., Pearson N.J., O'Reilly S.Y., 2008 GLITTER: Data reduction software for laser ablation ICP-MS. In Sylvester, P. (Ed.), Laser Ablation ICP-MS in the Earth Sciences: Current Practices and Outstanding Issues: Mineralogical Association of Canada, Short Course Series 40, 307–311.

Han, B.F., Wang, S.G., Jahn, B.M., Hong, D.W., Kagami, H., Sun, Y.L., 1997. Depleted-mantle source for the Ulungur River A-type granites from North Xinjiang, China: geochemistry and Nd–Sr isotopic evidence, and implications for Phanerozoic crustal growth. Chemical Geology 138, 135–159.

Han, B.F., Guo, Z.J., Zhang, Z.C., Zhang, L., Chen, J.F., Song, B., 2010. Age, geochemistry, and tectonic implications of a late Paleozoic stitching pluton in the North Tian Shan suture zone, western China. Bulletin 122, 627–640.

Harris, N.B., Pearce, J.A., Tindle, A.G., 1986. Geochemical characteristics of collision-zone magmatism. Geological Society, London, Special Publications 19, 67–81.

Hollister, L.S., 1993. The role of melt in the uplift and exhumation of orogenic belts. Chemical Geology 108, 31–48.

Hu, A., Jahn, B.M., Zhang, G., Chen, Y., Zhang, Q., 2000. Crustal evolution and Phanerozoic crustal growth in northern Xinjiang: Nd isotopic evidence. Part I. Isotopic characterization of basement rocks. Tectonophysics 328, 15–51.

Irvine, T.N.J., Baragar, W.R.A.F., 1971. A guide to the chemical classification of the common volcanic rocks. Canadian Journal of Earth Sciences 8, 523-548.

Jacobsen, S.B., Wasserburg, G.J., 1984. Sm-Nd isotopic evolution of chondrites and achondrites, II. Earth and Planetary Science Letters 67, 137–150.

Jahn, B., Wu, F., Chen, B., 2000. Granitoids of the Central Asian Orogenic Belt and continental growth in the Phanerozoic. Transactions of the Royal Society of Edinburgh 91, 181–193.

Jenner, G.A., Longerich, H.P., Jackson, S.E., Fryer, B.J., 1990. ICP-MS as a powerful tool for high precision trace element analysis in earth sciences: evidence from analysis of selected U.S.G.S. reference samples. Chemical Geology 83, 133–148.

Jochum, K.P., Nohl, U., 2008. Reference materials in geochemistry and environmental research and the GeoReM database. Chemical Geology 253, 50–53.

Johnston, A.D., Wyllie, P.J., 1988. Interaction of granitic and basic magmas: experimental observations on contamination processes at 10 kbar with H_2O. Contributions to Mineralogy and Petrology 98, 352–362.

Johnson, K., Barnes, C.G., Miller, C.A., 1997. Petrology, geochemistry, and genesis of high-Al tonalite and trondhjemites of the Cornucopia stock, Blue Mountains, Northeastern Oregon. Journal of Petrology 38, 1585–1611.

Karsli, O., Dokuz, A., Uysal, I., Aydin, F., Kandemir, R., Wijbrans, J., 2011. Generation of the Early Cenozoic adakitic volcanism by partial melting of mafic lower crust, Eastern Turkey: implications for crustal thickening to delamination. Lithos 114, 109–120.

Kay, R.W., Kay, S.M., 1993. Delamination and delamination magmatism. Tectonophysics 219, 177–189.

Khromykh, S.V., Vladimirov, A.G., Izokh, A.E., Travin, A.V., Prokop'ev, I.R., Azimbaev, E., Lobanov, S.S., 2013. Petrology and geochemistry of gabbro and picrites from the Altai collisional system of Hercynides: Evidence for the activity of the Tarim plume. Russian Geology and Geophysics 54, 1288–1304.

Khromykh, S.V., Tsygankov, A.A., Kotler, P.D., Navozov, O.V., Kruk, N.N., Vladimirov, A.G., Buyantuev, M.D., 2016. Late Paleozoic granitoid magmatism of Eastern Kazakhstan and Western Transbaikalia: plume model test. Russian Geology and Geophysics 57, 773–789.

Khromykh, S.V., Tsygankov, A.A., Burmakina, G.N., Kotler, P.D., Sokolova, E.N., 2018. Mantle-crust interaction in petrogenesis of the gabbro-granite association in the Preobrazhenka intrusion, Eastern Kazakhstan. Russian Petrology 26, 368–388.

Khubanov, V.B., Buyantuev, M.D., Tsygankov, A.A., 2016. U–Pb dating of zircons from PZ 3–MZ igneous complexes of Transbaikalia by sector-field mass spectrometry with laser sampling: technique and comparison with SHRIMP. Russian Geology and Geophysics 57, 190–205.

King, P.L., White, A.J.R., Chappell, B.W., 1997. Characterization and origin of aluminous A type granites of the Lachlan Fold Belt, southeastern Australia. Journal of Petrology 36, 371–391.

King, P.L., Chappell, B.W., Allen, C.M., White, A.J.R., 2001. Are A-type granites the high-temperature felsic granites? Evidence from fractionated granites of the Wangrah Suite. Australian Journal of Earth Sciences, 48, 501–514.

Koester, E., Pawley, A.R., Fernandes, L.A., Porcher, C.C., Soliani Jr,E., 2002. Experimental melting of cordierite gneiss and the petrogenesis of syntranscurrent peraluminous granites in southern Brazil. Journal of Petrology 43, 1595–1616.

Konnikov, E.G., Yermolov, P.V., Dobretsov, G.L., 1977. Petrology and Syn-inversional Gabbro-granitic Series. Nauka, Novosibirsk (in Russian).

Kotler, P.D., Khromykh, S.V., Vladimirov, A.G., Navozov, O.V., Travin, A.V., Karavaeva, G.S., Murzintsev, N.G., 2015. New data on the age and geodynamic interpretation of the Kalba-Narym granitic batholith, eastern Kazakhstan. Doklady Earth Sciences 462, 565–569.

Kröner, A., Kovach, V., Belousova, E., Hegner, E., Armstrong, R., Dolgopolova, A., Sun, M., 2014. Reassessment of continental growth during the accretionary history of the Central Asian Orogenic Belt. Gondwana Research 25, 103–125.

Kuibida, M.L., Kruk, N.N., Vladimirov, A.G., Polyanskii, N.V., Nikolaeva, I.V., 2009. U-Pb isotopic age, composition, and sources of the plagiogranites of the Kalba range, Eastern Kazakhstan. Doklady Earth Sciences 424, 72–76.

Kuibida, M.L., Kruk, N.N., Volkova, N.I., Serov, P.A., Velivetskaya, T.A., 2012. Composition, sources, and genesis of granitoids in the Irtysh Complex, Eastern Kazakhstan. Russian Petrology 20, 188–203.

Kuibida, M., Kruk, N., Murzin, O., Shokal'skii, S., Gusev, N., Kirnozova, T., Travin, A., 2013. Geologic position, age, and petrogenesis of plagiogranites in northern Rudny Altai. Russian Geology and Geophysics 54, 1305–1318.

Kuibida, M.L., Safonova, I.Y., Yermolov, P.V., Vladimirov, A.G., Kruk, N.N., Yamamoto, S., 2016. Tonalites and plagiogranites of the Char suture-shear zone in East Kazakhstan: Implications for the Kazakhstan-Siberia collision. Geoscience Frontiers 7, 141–150.

Küster, D., Harms, U., 1998. Post-collisional potassic granitoids from the southern and northwestern parts of the Late Neoproterozoic East African Orogen: a review. Lithos 45, 177–195.

Kuzebny V.S., 1975 Igneous Rocks of Southwestern Altai and their Metallogeny. Nauka KazSSR, Alma-Ata (in Russian).

Le Maitre, R.W.B., Dudek, P., Keller, A., Lameyre, J., Le Bas, J., Sabine, M.J., Zanettin, A.R., 1989. A classification of igneous rocks and glossary of terms: Recommendations of the International Union of Geological Sciences, Subcommission on the Systematics of Igneous Rocks, 552.3 CLA. International Union of Geological Sciences.

Li, P., Sun, M., Rosenbaum, G., Jourdan, F., Li, S., & Cai, K., 2017. Late Paleozoic closure of the Ob-Zaisan Ocean along the Irtysh shear zone (NW China): Implications for arc amalgamation and oroclinal bending in the Central Asian orogenic belt. Bulletin, 129, 547-569.

Liégeois, J.P., Navez, J., Hertogen, J., Black, R., 1998. Contrasting origin of post-collisional high-K calc-alkaline and shoshonitic versus alkaline and peralkaline granitoids. The use of sliding normalization. Lithos 45, 1–28.

Liew, T.C., Hofmann, A.W., 1998. Precambrian crustal components, plutonic associations, plate environment of the Hercynian Fold Belt of central Europe: indications from an Nd and Sr isotopic study. Contributions to Mineralogy and Petrology 98, 129–138.

Liu, B., Chen, J.F., Ma, X., Liu, J.L., Gong, E.P., Shi, W.G., Han, B.F., 2017. Timing of the final closure of the Irtysh–Zaysan Ocean: New insights from the earliest stitching pluton in the northern West Junggar, NW China. Geological Journal, http://dx.doi.org/10.1002/gj.3121.

Lopatnikov, V.V., Izokh, E.P., Ermolov, P.V., Ponomareva, A.P., Stepanov, A.S., 1982. Magmatism and Ore Potential of the Kalba-Narym Zone of East Kazakhstan, Nauka, Moscow (in Russian).

Lopez, S., Castro, A., Garcна-Casco, A., 2005. Production of granodiorite melt by interaction between hydrous mafic magma and tonalitic crust. Experimental constraints and implications for the generation of Archaean TTG complexes. Lithos 79, 229–250.

Ludwig, K.R., 2003. User's manual for Isoplot 3.00: a geochronological toolkit for Microsoft Excel, 4.

Martin, H., Smithies, R.H., Rapp, R., Moyen, J.F., Champion, D., 2005. An overview of adakite, tonalite–trondhjemite–granodiorite (TTG), and sanukitoid: relationships and some implications for crustal evolution. Lithos 79, 1–24.

Martin, R.F., 2006. A-type granites of crustal origin ultimately result from open-system fenitization-type reactions in an extensional environment. Lithos 91, 125–136.

McDonough, W.F., Sun, S.S., Ringwood, A.E., Jagoutz, E., Hofmann, A.W., 1992. Potassium, rubidium, and cesium in the Earth and Moon and the evolution of the mantle of the Earth. Geochimica et Cosmochimica Acta 56, 1001–1012.

Middlemost, E.A., 1994. Naming materials in the magma/igneous rock system. Earth-Science Reviews 37, 215–224.

Montel, J.M., Vielzeuf, D., 1997. Partial melting of metagreywackes, Part II. Compositions of minerals and melts. Contributions to Mineralogy and Petrology 128, 176–196.

Mossakovsky, A.A., Ruzhentsev, S.V., Samygin, S.G., Kheraskova, T.N., 1993. Central Asian fold belt: geodynamic evolution and history of formation. Russian Geotektonika 6, 3–33.

Moyen, J.-F., Martin, H., 2012. Forty years of TTG research. Lithos 148, 312–336.

Muir, R.J., Weaver, S.D., Bradshaw, J.D., Eby, G.N., Evans, J.A., 1995. The Cretaceous Separation Point batholith, New Zealand: granitoid magmas formed by melting of mafic lithosphere. Journal of the Geological Society 152, 689–701.

O'Connor, J.T., 1965. A classification for quartz-rich igneous rocks based on feldspar ratios. U.S. Geological Survey Professional Paper 525B, 79–84.

Orihashi, Y., Hirata, T., 2003. Rapid quantitative analysis of Y and REE abundances in XRF glass bead for selected GSJ reference rock standards using Nd-YAG 266 nm UV laser ablation ICP-MS. Geochemical Journal 37, 401–412.

Pattison, D.R., Chacko, T., Farquhar, J., McFarlane, C.R., 2003. Temperatures of granulite-facies metamorphism: constraints from experimental phase equilibria and thermobarometry corrected for retrograde exchange. Journal of Petrology 44, 867–900.

Pearce, J.A., Harris, N.B.W., Tindle, A.G., 1984. Trace element discrimination diagrams for the tectonic interpretation of granitic rocks. Journal of Petrology 25, 956–983.

Peccerillo, A., Taylor, S.R., 1976. Geochemistry of Eocene calc-alkaline volcanic rocks from the Kastamonu area, northern Turkey. Contributions to Mineralogy and Petrology 58, 63–81.

Petford, N., Atherton, M., 1996. Na-rich partial melts from newly underplated basaltic crust: the Cordillera Blanca Batholith, Peru. Journal of Petrology 37, 1491–1521.

Plotnikov A.V., Kruk N.N., Vladimirov V.G., Kovach V.P., Zhuravlev D.Z., Moroz E.N., 2003. Sm-Nd isotope systematics of metamorphic rocks western part of the Altai-Sajan folded area. Doklady Akad. Nauk 388, 228–232.

Rapp, R.P., Watson, E.B., 1986. Monazite solubility and dissolution kinetics: implications for the thorium and light rare earth chemistry of felsic magmas. Contributions to Mineralogy and Petrology 94, 304–316.

Rapp, R.P., Watson, E.B., 1995. Partial melting of metabasalt at 8-32 kbar: implications for continental growth and crustal-mantle recycling. Journal of Petrology 36, 891–931.

Rapp, R.P., Shimizu, N., Norman, M.D., 2003. Growth of early continental crust by partial melting of eclogite. Nature 425, 605–609.

Rickwood, P.C., 1989. Boundary lines within petrologic diagrams which use oxides of major and minor elements. Lithos 22, 247–263.

Roberts, M.P., Clemens, J.D., 1993. Origin of high-potassium, calc-alkaline, I-type granitoids. Geology 21, 825–828.

Rollinson, H.R., Tarney, J., 2005. Adakites–the key to understanding LILE depletion in granulites. Lithos 79, 61–81.

Rutter, M.J., Wyllie, P.J., 1988. Melting of vapour-absent tonalite at 10 kbar to simulate dehydration–melting in the deep crust. Nature 331, 159-160.

Safonova, I.Y., Seltmann, R., Kroner, A., Gladkochub, D., Schulmann, K., Xiao, W., Kim, T., Komiya, T., Sun, M., 2011. A new concept of continental construction in the Central Asian Orogenic Belt (compared to actualistic examples from the Western Pacific). Episodes 34, 186–194.

Safonova, I.Y., Simonov, V.A., Kurganskaya, E.V., Obut, O.T., Romer, R.L., Seltmann, R., 2012. Late Paleozoic oceanic basalts hosted by the Char suture-shear zone, East Kazakhstan: geological position, geochemistry, petrogenesis and tectonic setting. Journal of Asian Earth Sciences 49, 20–39.

Safonova, I., Maruyama, S., Kruk, N., Obut, O., Kotler, P., Gavryushkina, O., Khromykh S.V., Kuibida M., Krivonogov, S., 2018a. Pacific-type orogenic belts: linking evolution of oceans, active margins and intra-plate magmatism. Episodes, 41, 78-87.

Safonova, I.Y., Komiya, T., Romer, R. L., Simonov, V., Seltmann, R., Rudnev, Yamamoto, S., Sun, M., 2018b. Supra-subduction igneous formations of the Char ophiolite belt, East Kazakhstan. Gondwana Research 59, 159-179.

Scherba, G.N., D'yachkov, B.A., Stuchevsky, N.I., Nakhtigal, G.P., Antonenko, A.N., Lubetsky, V.N., 1998. The Great Altai (Geology and Metallogeny). Book 1. Gylym, Almaty (in Russian).

Sen, C., Dunn, T., 1994. Dehydration melting of a basaltic composition amphibolite at 1.5 and 2.0 GPa: implications for the origin of adakites. Contributions to Mineralogy and Petrology 117, 394–409.

Şengör, A.M.C., Natal'in, B.A., Burtman, V.S., 1993. Evolution of the Altaid tectonic collage and Paleozoic crustal growth in Eurasia. Nature 364, 299–307.

Shand, S.J., 1943. Eruptive Rocks: Their genesis, Composition, and Classification, with a Chapter on Meteorites. Wiley & Sons, New York.

Shen, P., Shen, Y., Liu, T., Li, G., Zeng, Q., 2008. Geology and geochemistry of the Early Carboniferous Eastern Sawur caldera complex and associated gold epithermal mineralization, Sawur Mountains, Xinjiang, China. Journal of Asian Earth Sciences 32, 259–279.

Shen, X., Zhang, H., Wang, Q., Wyman, D.A., Yang, Y., 2011. Late Devonian–Early Permian A-type granites in the southern Altay Range, Northwest China: petrogenesis and implications for tectonic setting of "A2-type" granites. Journal of Asian Earth Sciences 42, 986–1007.

Singh, J., Johannes, W., 1996. Dehydration melting of tonalites. Part II. Composition of melts and solids. Contributions to Mineralogy and Petrology 125, 26–44.

Skjerlie, K.P., Johnston, A.D., 1992. Vapor-absent melting at 10 kbar of a biotite-and amphibole-bearing tonalitic gneiss: implications for the generation of A-type granites. Geology 20, 263–266.

Skjerlie, K.P., Douce, A.E.P., Johnston, A.D., 1993. Fluid absent melting of a layered crustal protolith: implications for the generation of anatectic granites. Contributions to Mineralogy and Petrology 114, 365–378.

Skjerlie, K.P., Douce, A.P., 1995. Anatexis of interlayered amphibolite and pelite at 10 kbar: effect of diffusion of major components on phase relations and melt fraction. Contributions to Mineralogy and Petrology 122, 62–78.

Smithies, R.H., 2000. The Archaean tonalite–trondhjemite–granodiorite (TTG) series is not an analogue of Cenozoic adakite. Earth and Planetary Science Letters 182, 115–125.

Song, Y., Xu, H., Zhang, J., Wang, D., Liu, E., 2014. Syn-exhumation partial melting and melt segregation in the Sulu UHP terrane: Evidences from leucosome and pegmatitic vein of migmatite. Lithos 202, 55–75.

Spicer, E.M., Stevens, G., Buick, I.S., 2004. The low-pressure partial-melting behaviour of natural boron-bearing metapelites from the Mt. Stafford area, central Australia. Contributions to Mineralogy and Petrology 148, 160–179.

Stevens, G., Villaros, A., Moyen, J.F., 2007. Selective peritectic garnet entrainment as the origin of geochemical diversity in S-type granites. Geology 35, 9–12.

Sun, S.S., McDonough, W.S., 1989. Chemical and isotopic systematics of oceanic basalts: implications for mantle composition and processes. Geological Society, London, Special Publications 42, 313–345.

Sun, S., McDonough, W.F., 1989. Chemical and isotopic systematics of oceanic basalts: Implications for mantle composition and processes. In: Saunders, A.D., Norry, M.J. (Eds.), Magmatism in the Ocean Basins, Journal of the Geological, Society, London, Special Publication 42, 313–345.

Sylvester, P.J., 1989. Post-collisional alkaline granites. The Journal of Geology 97, 261–280.

Tate, M.C., Johnson, S.E., 2000. Subvolcanic and deep-crustal tonalite genesis beneath the Mexican Peninsular Ranges. The Journal of Geology 108, 721–728.

Sylvester, P.J., 1998. Post-collisional strongly peraluminous granites. Lithos 45, 29–44.

Turkina, O.M., 2005. Proterozoic tonalites and trondhjemites of the southwestern margin of the Siberian craton: isotope geochemical evidence for the lower crustal sources and conditions of melt formation in collisional settings. Russian Petrology 13, 35–48.

Vanderhaeghe, O., 2009. Migmatites, granites and orogeny: Flow modes of partially-molten rocks and magmas associated with melt/solid segregation in orogenic belts. Tectonophysics 477, 119–134.

Vielzeuf, D., Montel, J.M., 1994. Partial melting of metagreywackes. Part I. Fluid-absent experiments and phase relationships. Contributions to Mineralogy and Petrology 117, 375–393.

Vladimirov, A.G., Kozlov, M.S., Shokalsky, S.P., Khalilov, V.A., Rudnev, S.N., Kruk, N.N., Vystavnoi, S.A., Borisov, S.M., Berezikov, Yu.K., Metsner, A.N., Babin, G.A., Mamlin, A.N., Murzin, O.M., Nazarov, G.V., Makarov, V.A., 2001. Major epochs of intrusive magmatism of Kuznetsk Alatau, Altai, and Kalba (from U-Pb isotope dates), Russian Geology and Geophysics 42, 1157–1178.

Vladimirov, A.G., Kruk, N.N., Rudnev, S.N., Khromykh, S.V., 2003. Geodynamics and granitoid magmatism of collision orogens. Russian Geology and Geophysics 44, 1321–1338.

Vladimirov, A.G., Kruk, N.N., Khromykh, S.V., Polyansky, O.P., Chervov, V.V., Vladimirov, V.G., Travin, A.V., Babin, G.A., Kuibida, M.L., Khomyakov, V.D., 2008. Permian magmatism and lithospheric deformation in the Altai caused by crustal and mantle thermal processes. Russian Geology and Geophysics 49, 468–479.

Volkova, N.I., Sklyarov, E.V., 2007. High-pressure complexes of the Central Asian Fold Belt: geological setting, geochemistry, and geodynamic implications. Russian Geology and Geophysics 48, 83–90.

Volkova, N.I., Tarasova, E.N., Polyanskii, N.V., Vladimirov, A.G., Khomyakov, V.D., 2008. High-pressure rocks in the serpentinite mйlange of the Chara zone, eastern Kazakhstan: Geochemistry, petrology, and age. Geochemistry International 46, 386–401.

Wang, Q., Xu, J.F., Jian, P., Bao, Z.W., Zhao, Z.H., Li, C.F., Xiong, X.L., Ma, J.L., 2006. Petrogenesis of adakitic porphyries in an extensional tectonic setting, Dexing, South China: implications for the genesis of porphyry copper mineralization. Journal of Petrology 47, 119–144.

Wang, B., Cluzel, D., Shu, L., Faure, M., Charvet, J., Chen, Y., De Jong, K., 2009. Evolution of calc-alkaline to alkaline magmatism through Carboniferous convergence to Permian transcurrent tectonics, western Chinese Tianshan. International Journal of Earth Sciences 98, 1275.

Watkins, J. M., Clemens, J. D., Treloar, P.J., 2007. Archaean TTGs as sources of younger granitic magmas: melting of sodic metatonalites at 0.6–1.2 GPa. Contributions to Mineralogy and Petrology 154, 91–110.

Watson, E.B., Harrison, T.M., 1983. Zircon saturation revisited: temperature and composition effects in a variety of crustal magma types. Earth and Planetary Science Letters 64, 295–304.

Whalen, J.B., Currie, K.L., Chappell, B.W., 1987. A-type granites: geochemical characteristics, discrimination and petrogenesis. Contributions to Mineralogy and Petrology 95, 407–419.

Whalen, J.B., Jenner, G.A., Longstaffe, F.J., Robert, F., Gariйpy, C., 1996. Geochemical and isotopic (O, Nd, Pb and Sr) constraints on A-type granite petrogenesis based on the Topsails igneous suite, Newfoundland Appalachians. Journal of Petrology 37, 1463–1489.

Whalen, J.B., Percival, J.A., McNICOLL, V.J., Longstaffe, F.J., 2002. A mainly crustal origin for tonalitic granitoid rocks, Superior Province, Canada: implications for late Archean tectonomagmatic processes. Journal of Petrology 43, 1551–1570.

White, R.V., Tarney, J., Kerr, A.C., Saunders, A.D., Kempton, P.D., Pringle, M.S., Klaver, G.T., 1999. Modification of an oceanic plateau, Aruba, Dutch Caribbean: implications for the generation of continental crust. Lithos 46, 43–68.

Windley, B.F., Alexeiev, D., Xiao, W., Kroner, A., Badarch, G., 2007. Tectonic models for accretion of the Central Asian Orogenic Belt. Journal of Geological Society London 164, 31–47.

Winther, K.T., 1996. An experimentally based model for the origin of tonalitic and trondhjemitic melts. Chemical Geology 127, 43–59.

Wolf, M.B., Wyllie, P.J., 1994. Dehydration-melting of amphibolite at 10 kbar: the effects of temperature and time. Contributions to Mineralogy and Petrology 115, 369–383.

Xiao, L., Clemens, J.D., 2007. Origin of potassic (C-type) adakite magmas: experimental and field constraints. Lithos 95, 399–414.

Xiao, W., Santosh, M., 2014. The western Central Asian Orogenic Belt: a window to accretionary orogenesis and continental growth. Gondwana Research 25, 1429–1444.

Xiao, W., Huang, B., Han, C., Sun, S., Li, J., 2010. A review of the western part of the Altaids: a key to understanding the architecture of accretionary orogens. Gondwana Research 18, 253–273.

Xiong, X.L., Li, X.H., Xu, J.F., Li, W.X., 2003. Extremely high Na adakite-like magmas derived from lower crust basaltic underplate: the Zhantang andesitic rocks from Huichang Basin, SE China. Geochemical Journal 37, 233–252.

Xiong, X.L., Adam, J., Green, T.H., 2005. Rutile stability and rutile/melt HFSE partitioning during partial melting of hydrous basalt: implications for TTG genesis. Chemical Geology 218, 339–359.

Yakubchuk, A.S., 2004. Architecture and mineral deposit settings of the Altaid orogenic collage: a revised model. Journal of Asian Earth Sciences 23, 761–779.

Yang, G., Li, Y., Wu, H., Zhong, X., Yang, B., Yan, C., Si, G., 2011. Geochronological and geochemical constrains on petrogenesis of the Huangyangshan A-type granite from the East Junggar, Xinjiang, NW China. Journal of Asian Earth Sciences 40, 722–736.

Yermolov, P.V., Dobretsov, N.L., Polyansky, N.V., Klenina, N.L., Khomyakov, V.D., Kuzebny, V.S., Revyakin, P.S., Bortsov, V.D., 1981. Ophiolites of the Chara zone. In: Abdulin, A.A., Patalakha, E.I. (Eds.), Ophiolites. Nauka KazSSR, Alma-Ata, 103–178 (in Russian).

Yermolov, P.V., Vladimirov, A.G., Izokh, A.E., Polyansky, N.V., Kuzebnyi, B.C., Revyakin, P.S., Bortsov, V.D., 1983. Orogenic Magmatism of Ophiolite Belts (by example of East Kazakhstan), Nauka, Novosibirsk (in Russian).

Yermolov, P.V., 2013. Key Problems of the Isotope Geology and Metallogeny of Kazakhstan. Kazakhstan-Russian University Publ., Karaganda (in Russian).

Yin, J., Yuan, C., Sun, M., Long, X., Zhao, G., Wong, K. P., Cai, K., 2010. Late Carboniferous high-Mg dioritic dikes in Western Junggar, NW China: geochemical features, petrogenesis and tectonic implications. Gondwana Research 17, 145–152.

Yuan, C., Sun, M., Xiao, W., Li, X., Chen, H., Lin, S., Long, X., 2007. Accretionary orogenesis of the Chinese Altai: insights from Paleozoic granitoids. Chemical Geology 242, 22–39.

Yuan, C., Sun, M., Wilde, S., Xiao, W.J., Xu, Y.G., Long, X.P., Zhao, G.C., 2010. Post-collisional plutons in the Balikun area, East Chinese Tianshan: evolving magmatism in response to extension and slab break-off. Lithos 119, 269–288.

Yuan, L., Zhang, X., Xue, F., Liu, F., 2016. Juvenile crustal recycling in an accretionary orogen: Insights from contrasting Early Permian granites from central Inner Mongolia, North China. Lithos 264, 524–539.

Zen, E. A., 1986. Aluminum enrichment in silicate melts by fractional crystallization: some mineralogic and petrographic constraints. Journal of Petrology 27, 1095–1117.

Zhang, C. L., Santosh, M., Zou, H. B., Xu, Y. G., Zhou, G., Dong G. F., Ding R. F., Wang, H. Y., 2012. Revisiting the "Irtish tectonic belt": Implications for the Paleozoic tectonic evolution of the Altai orogen. Journal of Asian Earth Sciences, 52, 117-133.

Zhang, X., Yuan, L., Xue, F., Yan, X., Mao, Q., 2015. Early Permian A-type granites from central Inner Mongolia, North China: Magmatic tracer of post-collisional tectonics and oceanic crustal recycling. Gondwana Research 28, 311–327.

Zhao, P., Jahn, B. M., Xu, B., Liao, W., Wang, Y., 2016. Geochemistry, geochronology and zircon Hf isotopic study of peralkaline-alkaline intrusions along the northern margin of the North China Craton and its tectonic implication for the southeastern Central Asian Orogenic Belt. Lithos 261, 92–108.

Zonenshain, L.P., Kuzmin, M.I., Natapov, L.M., 1990. Geology of the USSR: Plate Tectonic Synthesis. American Geophysical Union. Geodynamics Series Monograph, 21.

Figure captions

Fig. 1. Generalized geological map of the Kalba fold belt (modified after 1:500 000 Geological Map, *GRK "Topaz"*, Ust'-Kamenogorsk), illustrating the location of intrusions of the Kunush and Kalguty complexes. Age data are from: 1 – Khromykh et al. (2016); 2 – Khromykh et al. (2018); 3 – Kuibida et al. (2009); 4 – This study.

Fig. 2. Representative field photographs. (a-b) intrusions of the Kunush complex; (c-d) intrusions of the Kalguty complex.

Fig. 3. Representative cathodoluminescence images of zircons. (a-d) Kalguty high-K granitoids: (a) quartz-monzonite, early phase of the Kurchum intrusion (sample X-1052); (b) quartz-monzonite, late phase of the Kurchum Intrusion (sample X-1047); (c) granodiorite, Razdolny intrusion (sample MX-841); (d) quartz-monzonite porphyry, VDN-dyke (sample K-34/1). (e-g) Kunush high-Na granitoids: (e) granite porphyry, dyke near the Kunush intrusion (sample 7-694); (g) porphyritic granite, Besterek intrusion (sample K-14-104). For details of data selection see Section 4.1.

Fig. 4. U-Pb dating results and concordia diagrams for the selected ages. (a-d) Kalguty high-K granitoids: (a) quartz-monzonite, early phase of the Kurchum intrusion; (b) quartz-monzonite, late phase of the Kurchum Intrusion; (c) granodiorite, Razdolny intrusion; (d) quartz-monzonite porphyry, VDN-dyke. (e-g) Kunush high-Na granitoids: (e) granite porphyry, dyke near the Kunush intrusion; (g) porphyritic granite, Besterek intrusion. For details of data selection see Section 4.1.

Fig. 5. Micro-photos of representative granitoid samples selected for U-Pb dating. (a-d) Kunush high-Na granitoids: (a) massive granite, Zhilandy intrusion; (b) porphyritic granite,

Tochka intrusion; (c) porphyritic granite, Besterek intrusion; (d) granite porphyry, dyke near the Kunush intrusion. (e-h) Kalguty high-K granitoids: (e) quartz-monzonite, early phase of the Kurchum intrusion; (g) quartz-monzonite, late phase of the Kurchum intrusion; (f) granodiorite, Razdolny intrusion; (h) quartz-monzonite porphyry, VDN-dyke. Pl = plagioclase, Kfsp = K-feldspar, Qtz = quartz, Bt = biotite, Px = pyroxene. For details of data selection see Section 4.2.

Fig. 6. (a): An-Or-Ab diagram (O'Connor, 1965; Barker, 1979). Fields: To = tonalite, Tdh = trondhjemite, Grd = granodiorite, Gr = granite, Qm = qtz-monzonite. (b): Mg-Ca-Na triangle (elements are quoted in apfu.) for the Kunush high-Na granitoids, compared to slab-derived adakites (LSA- and HSA-type; SiO_2<60 and >60 wt.%, respectively; after Martin et al, 2005) from Kamchatka, Ecuador, Chile, Panama and the Honshu, Luzon, New Zeland, Tonga (GEOROC database); and lower crust adakite-like granitoids from New Zealand, China, Turkey, Japan and North America, after (Muir et al., 1995; Petford and Atherton, 1996; Johnson et al., 1997; Xiong et al., 2003; Karsli et al., 2011).

Fig. 7. Chondrite-normalized REE diagrams (Sun, McDonough, 1989) and Primitive mantle-normalized multielement diagrams (McDonough et al., 1992) for the Kunush high-Na (a-b) and Kalguty high-K (c) granitoids.

Fig. 8. Chemical classification of the Kurchum granitoids. (a): Total alkalis vs. Silica diagram (Le Maitre et al., 1989), division according to (Middlemost, 1994). (b): K_2O vs. SiO_2 alkalinity diagram (Rickwood, 1989). (c): Aluminum Saturation Index (Al/(Ca-1.67P+Na+K) molar ratio) vs. SiO_2 diagram (Shand, 1943). (d): $FeO^{tot}/(FeO^{tot}+MgO)$ vs. SiO_2 (wt.%) diagram for discrimination between ferroan and magnesian series (Frost et al., 2001).

Fig. 9. (a): (K_2O+Na_2O)/CaO vs. Zr+Nb+Ce+Y fields of *A*-type granites, fractionated granites (FG) and unfractionated *M*-, *I*- and *S*-type granites (OGT), after (Whalen et al.,1987; Sylvester, 1989). (b): Nb vs Y; c: Rb vs. Y+Nb tectonic discriminant diagram for granitic rocks (Pearce et al., 1984). SYN-COLG = syn-collisional granites, WPG = within-plate granites, ORG = ocean ridge granites, VAG = volcanic arc granites. (d): Zr (ppm) vs. SiO_2 (wt%) content for *A*- and *I*-type granites at Zr-saturated crystallization. The chemical trends show continuously decreasing Zr with increasing SiO_2 and indicating derivation from a quartz-feldspathic source and primary zircon saturation. *I*-type field includes meta- to peraluminous granites (King et al., 2001).

Fig. 10. εNd(t) vs. T_{DM} (Ma) age plot for the Kunush and Kalguty granitoids. Data for the Kalba fold belt and Irtysh Shear zone lithology are according to (Plotnikov et al, 2003; Kuibida et al., 2009; Hu et al., 2000; Yermolov, 2013); those for the Chara ophiolite zone NMORB+OIB are according to (Volkova et al., 2008; Safonova et al., 2012). For details of data selection see Table 4.

Fig. 11. (a): Kunush high-Na granitoids compared to adakites in Nb/Ta vs. Zr/Sm diagram (Condie et al., 2005). Lines are Primitive mantle values from (Sun and McDonough, 1989) and melting fields from (Foley et al., 2000). Modern HSA have chondritic Nb/Ta ratios (dashed field). High Nb/Ta reflect a rutile-present residue and correspond to higher melting depths. (b): Kunush high-Na granitoids compared to high, medium and low pressure TTGs (dark, grey and white dots, respectively) in Ta vs. Nb diagram (Moyen and Martin, 2012).

Fig. 12. Kalguty high-K granitoids compared to experimental melts from different sources, with a non-garnet residual phase and a melt fraction of 20-60%: metapelite (Douse and Beard, 1995; García-Casco, 2003; Spicer et al., 2004); gneiss (Douce and Beard, 1995; Castro et al., 1999; Koester, 2002); metagreywacke (Vielzeuf and Montel, 1994; Douce and Beard, 1996;

Montel and Vielzeuf, 1997) at < 10 kbar; gneiss + gabbro (Castro et al., 1999), gneiss + basalt (Douse et al., 1995), tonalite + synthetic mafic glass (Lopez et al., 2005) at 4-10 kbar; dacite, andesite (Conrad et al., 1988; Alonso–Perez et al., 2009) at 8-10 kbar; quartz-amphibolite (Douse and Beard, 1995) at 3-10 kbar; diorite, tonalite, granodiorite (Skjerlie and Johnston, 1992; Singh and Johannes, 1996; Douse, 1997) at 2-10 kbar. (a): Total alkalis vs. Silica diagram (Le Maitre et al., 1989), division according to (Middlemost, 1994). (b): K_2O vs. SiO_2 alkalinity diagram (Rickwood, 1989). (c): Aluminum Saturation Index (Al/(Ca-1.67P+Na+K) molar ratio) vs. SiO_2 diagram (Shand, 1943). (d): $FeO^{tot}/(FeO^{tot}+MgO)$ vs. SiO_2 (wt.%) diagram discriminating between ferroan and magnesian series (Frost et al., 2001). Abbreviations stand for *mp* = metapelite; *mgw* = metagreywacke; *gn* = gneiss; *dr* = diorite; *ton* = tonalite; *grd* = granodiorite; *and* = andesite; *dac* = dacite; *qm* = quartz-amphibolite; *mix* = heterogeneous protoliths. The experimental melts compositions with SiO_2 > 75 wt. % and *ASI* > 1.2 (gray color) were excluded because differ from the Kalguty granites values.

Fig. 13. Schematic cartoon illustrating the geodynamic evolution of the Irtysh-Zaisan orogen in the Late Carboniferous-Early Permian, modified after (Scherba et al., 1998; Vladimirov et al., 2008). (a) Continent–continent oblique collision and slab break-off induced granite magmatism at the Altai and Zharma-Saur active margin and Chara suture zone. (b) The oblique post-collisional interaction during continuing horizontal motion of the two plates relative to one another resulted to uplifting of mantle asthenosphere and thermal anomaly beneath the orogenic prism. Age data are from: 1-3 - Kuibida et al. (2013, 2016 and 2009, respectively); 4 - Khromykh et al. (2016); 5 - this study.

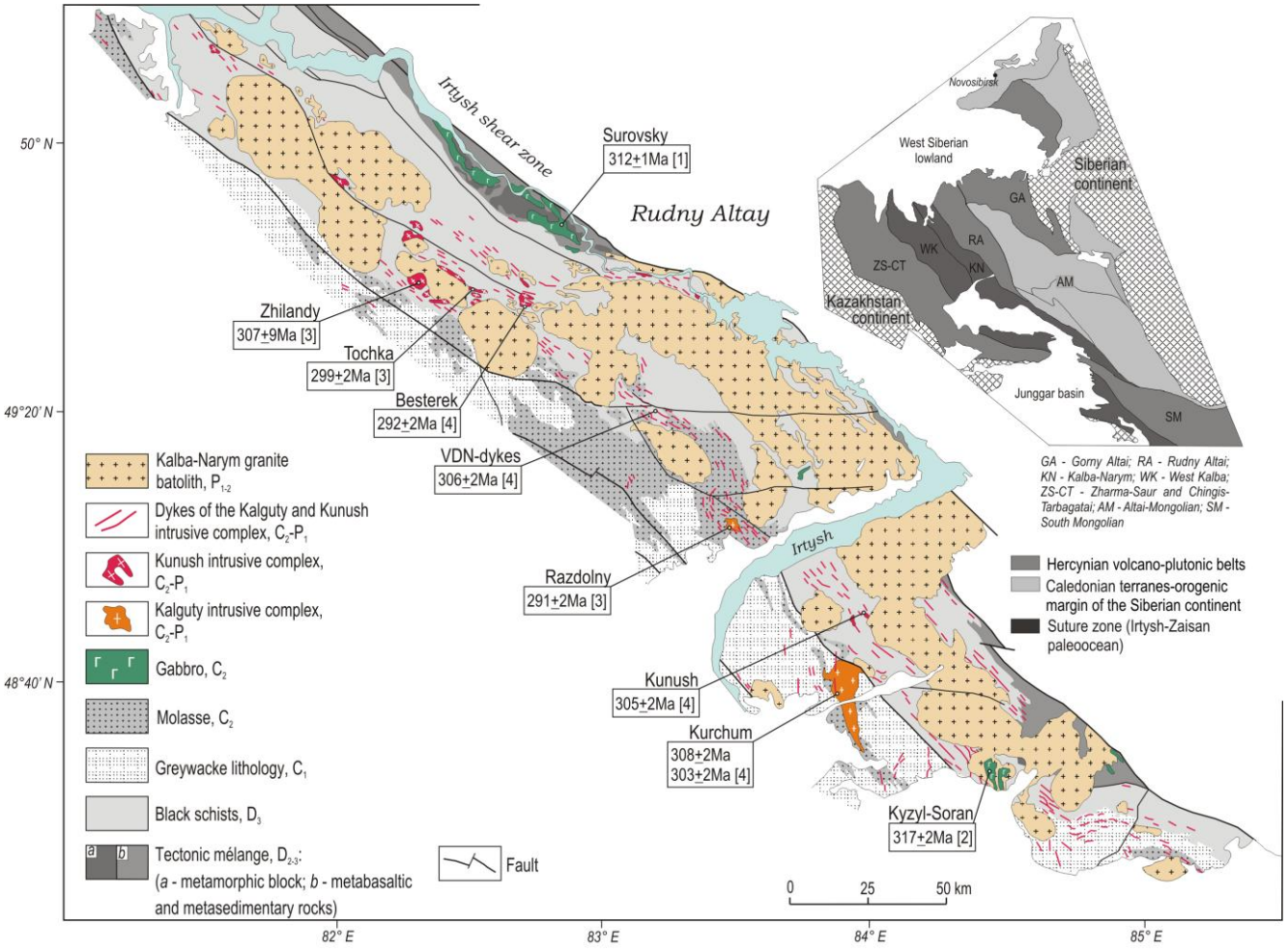

Figure 1.

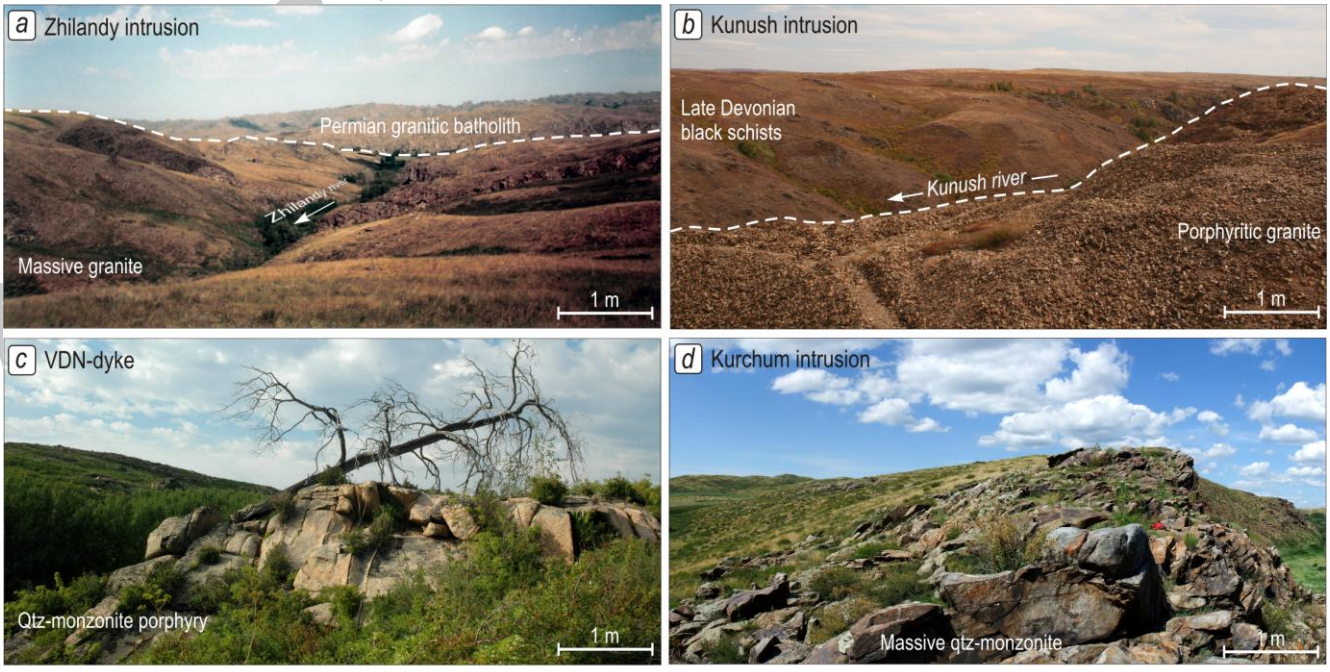

Figure 2.

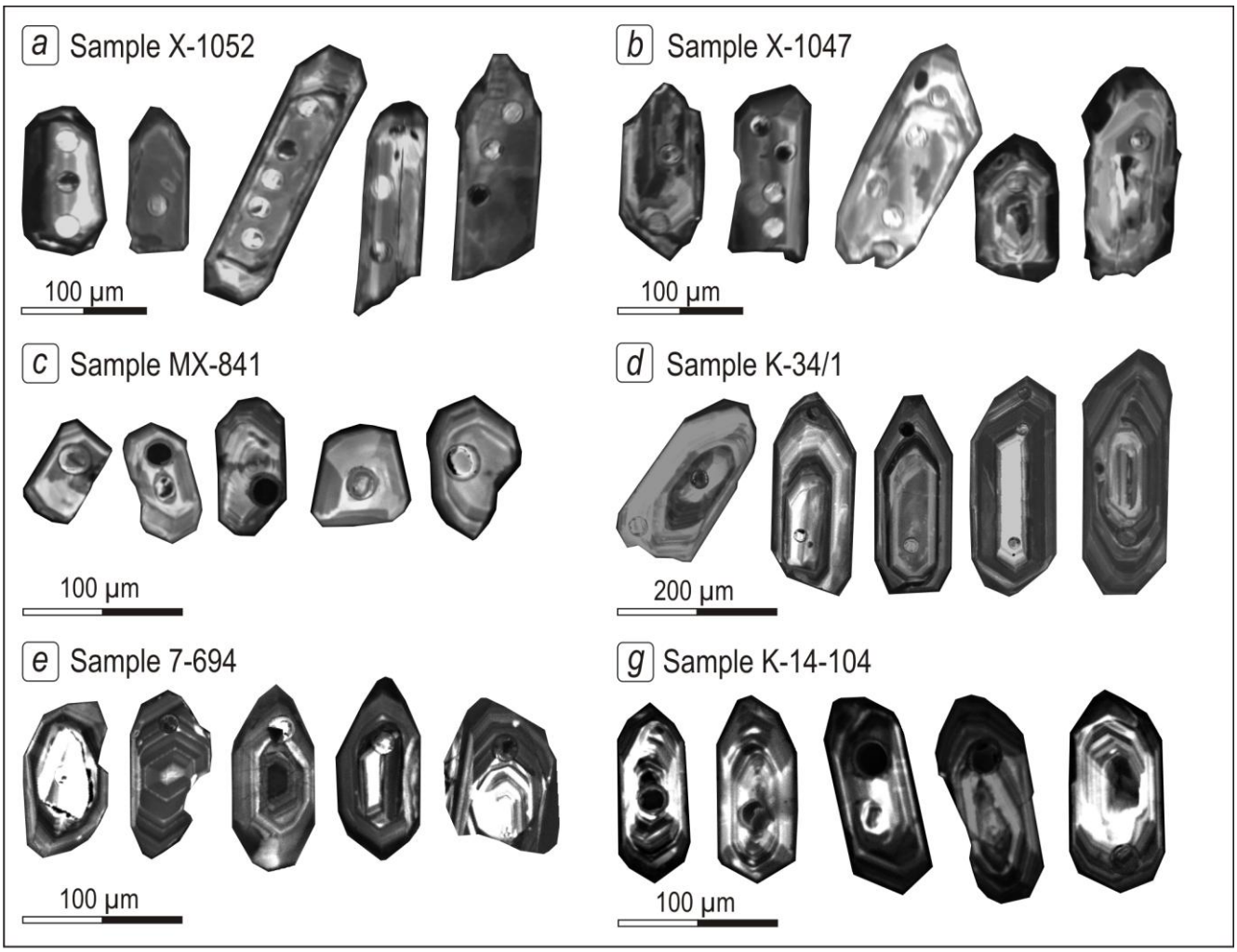

Figure 3.

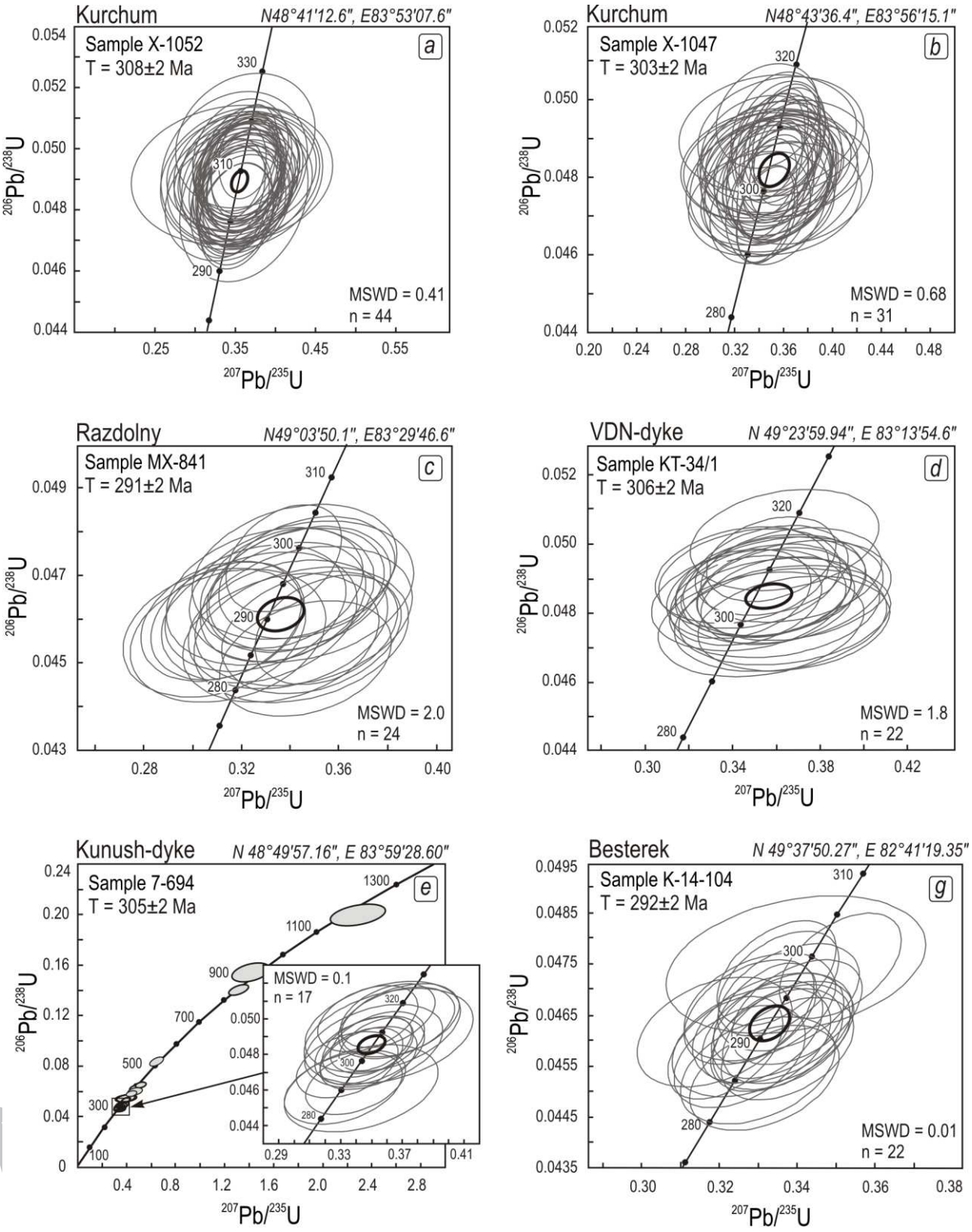
Kurchum
N48°41'12.6", E83°53'07.6"
Sample X-1052
T = 308±2 Ma
a
MSWD = 0.41
n = 44
Kurchum
N48°43'36.4", E83°56'15.1"
Sample X-1047
T = 303±2 Ma
b
MSWD = 0.68
n = 31
Razdolny
N49°03'50.1", E83°29'46.6"
Sample MX-841
T = 291±2 Ma
c
MSWD = 2.0
n = 24
VDN-dyke
N 49°23'59.94", E 83°13'54.6"
Sample KT-34/1
T = 306±2 Ma
d
MSWD = 1.8
n = 22
Kunush-dyke
N 48°49'57.16", E 83°59'28.60"
Sample 7-694
T = 305±2 Ma
e
MSWD = 0.1
n = 17
Besterek
N 49°37'50.27", E 82°41'19.35"
Sample K-14-104
T = 292±2 Ma
g
MSWD = 0.01
n = 22
206Pb/238U
207Pb/235U

Figure 4.

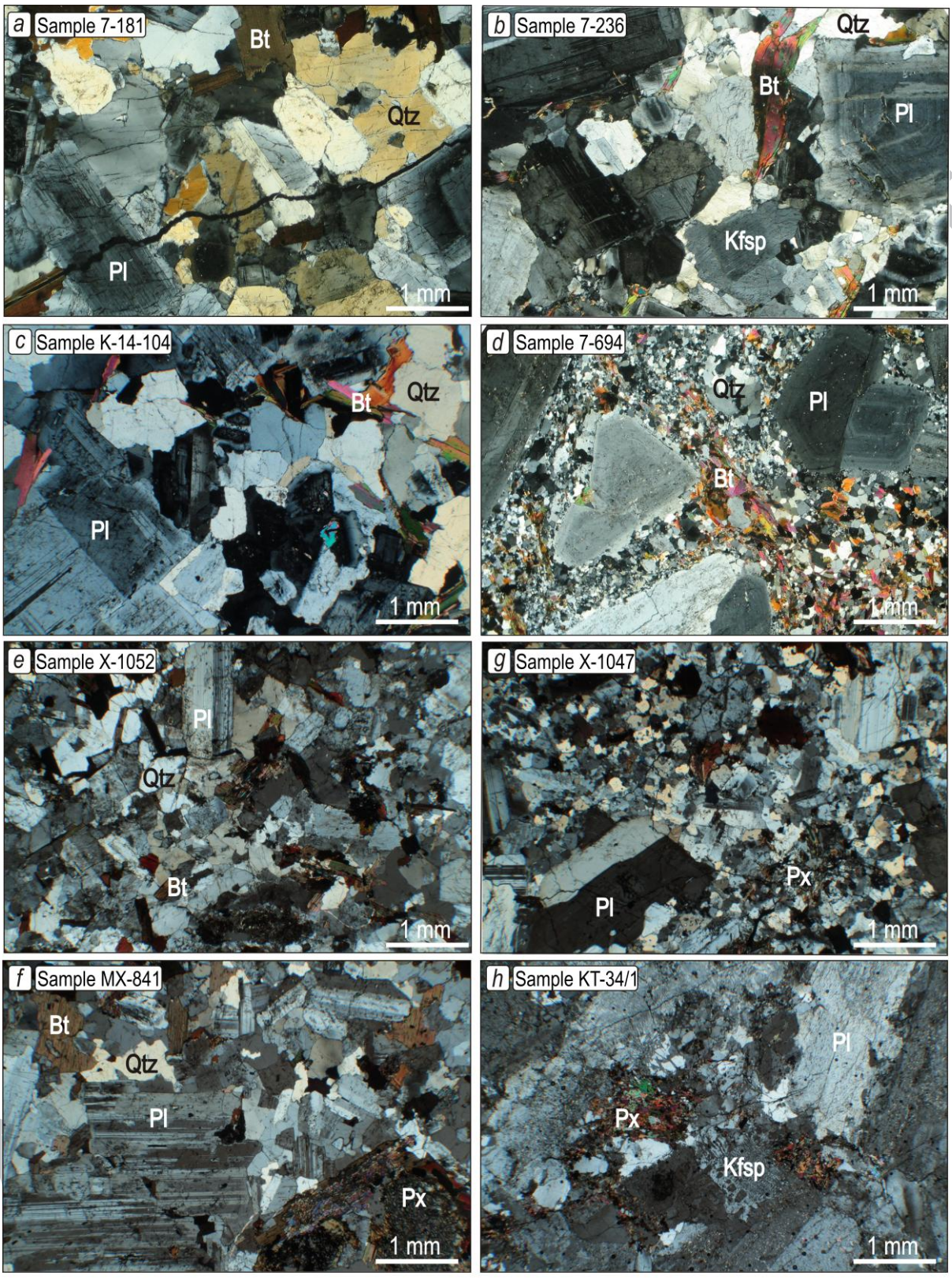

Figure 5.

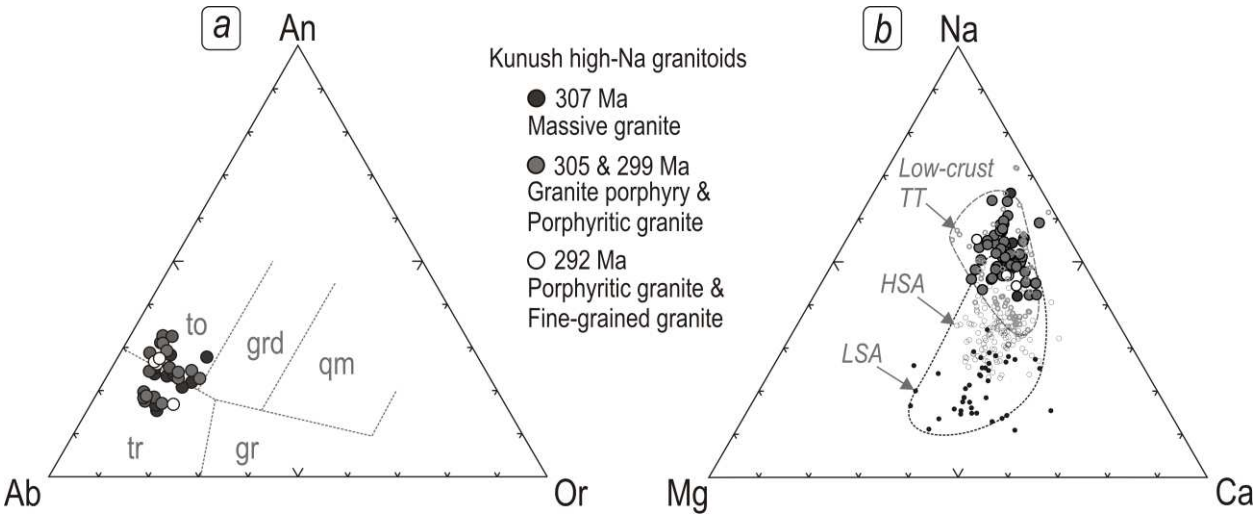

Figure 6.

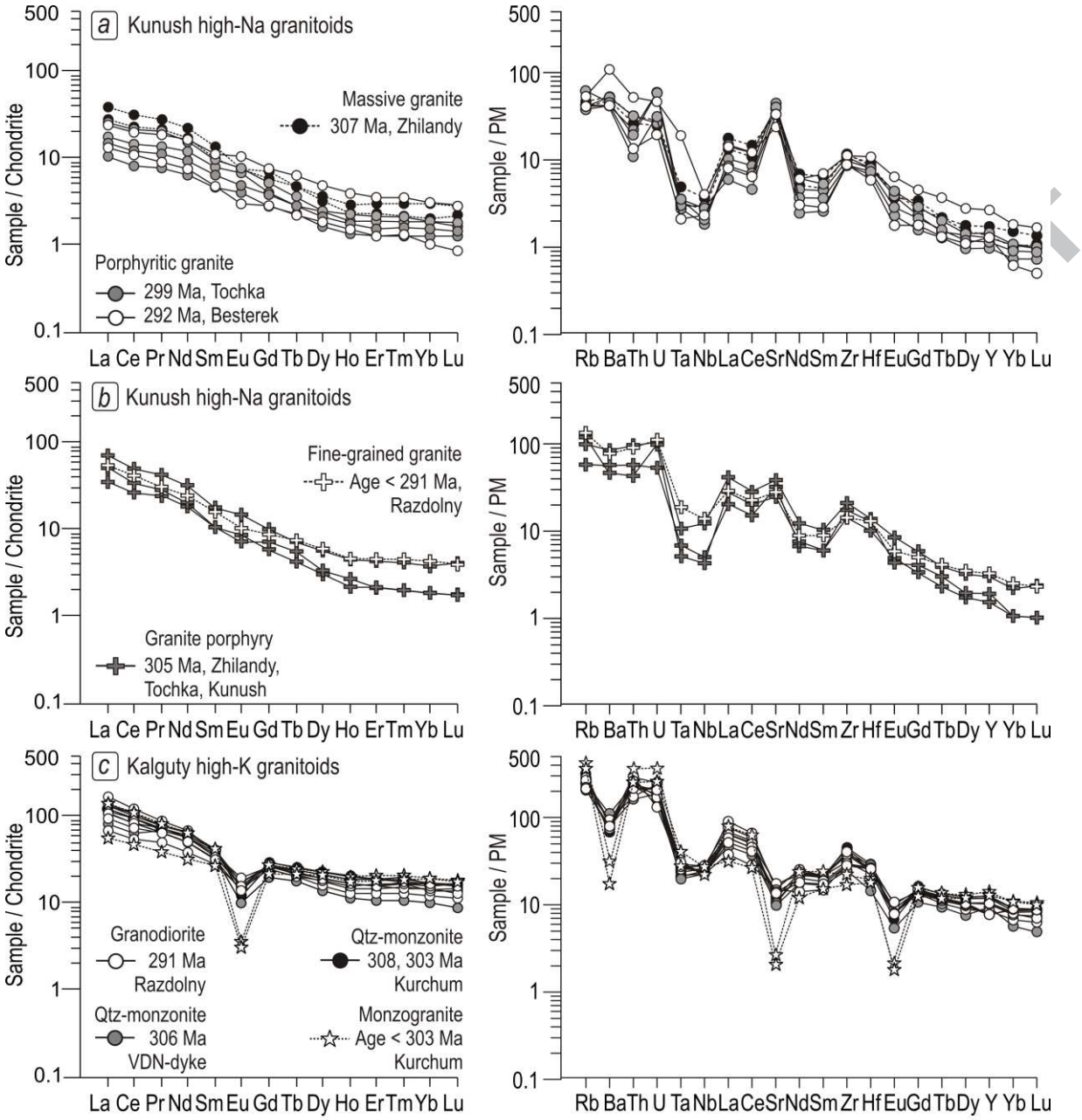

Figure 7.

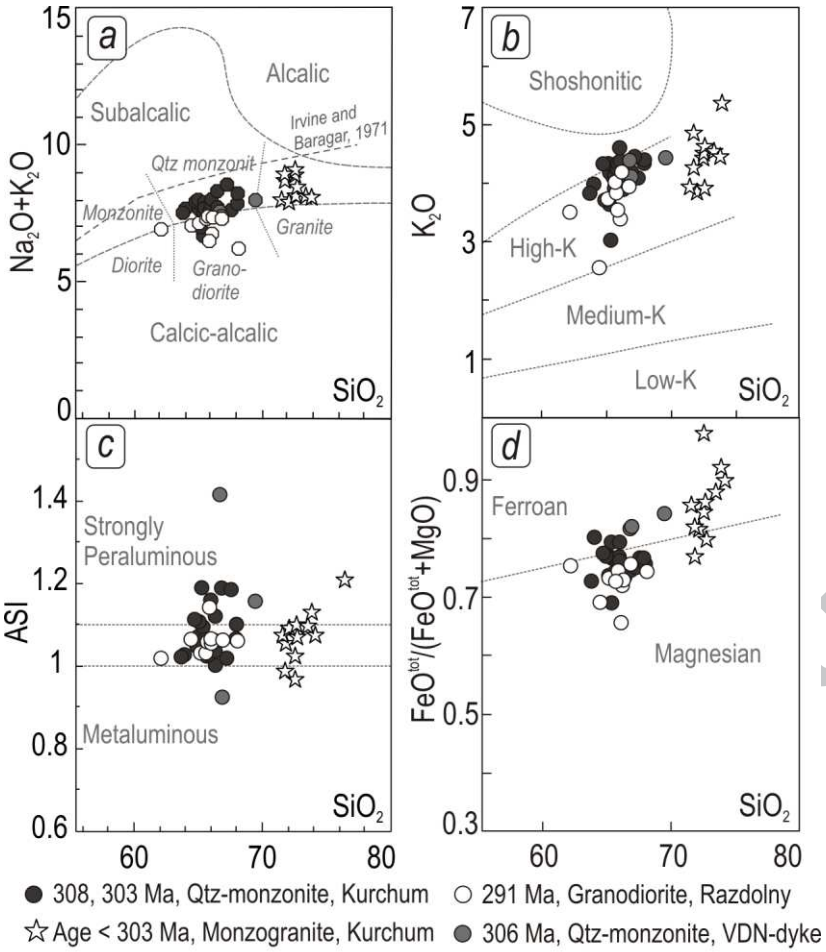

Figure 8.

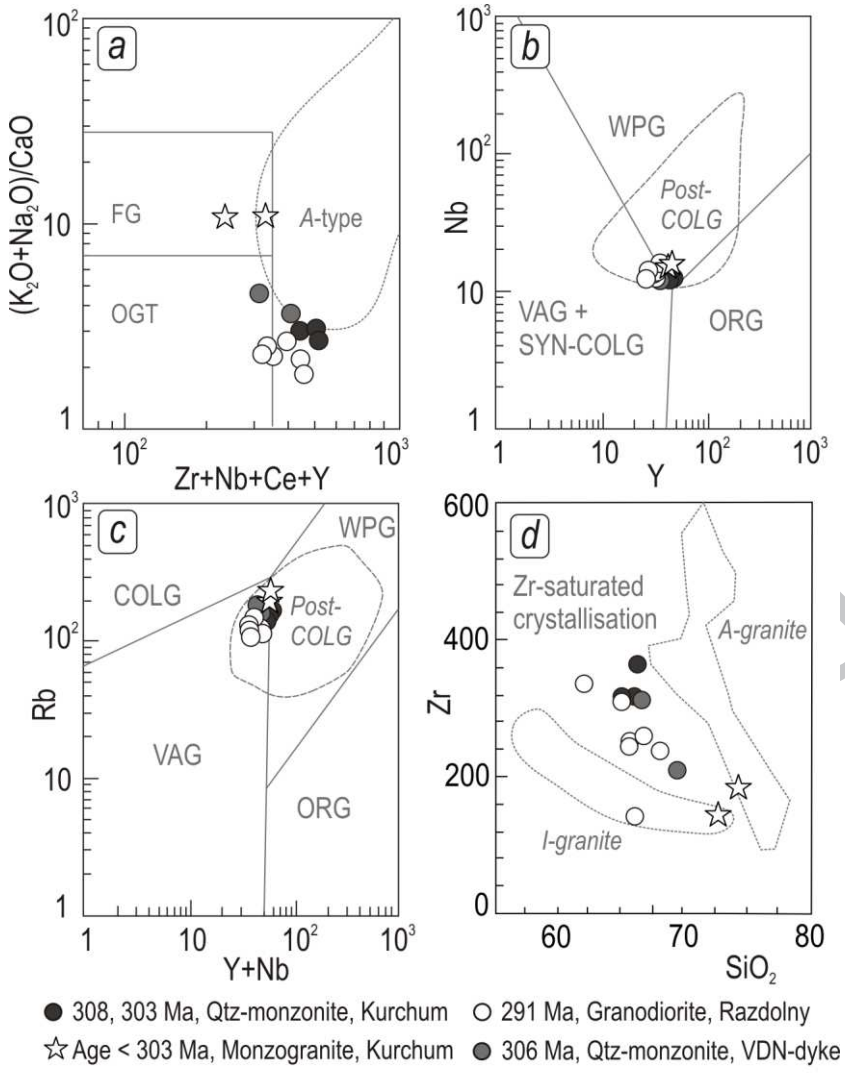

Figure 9.

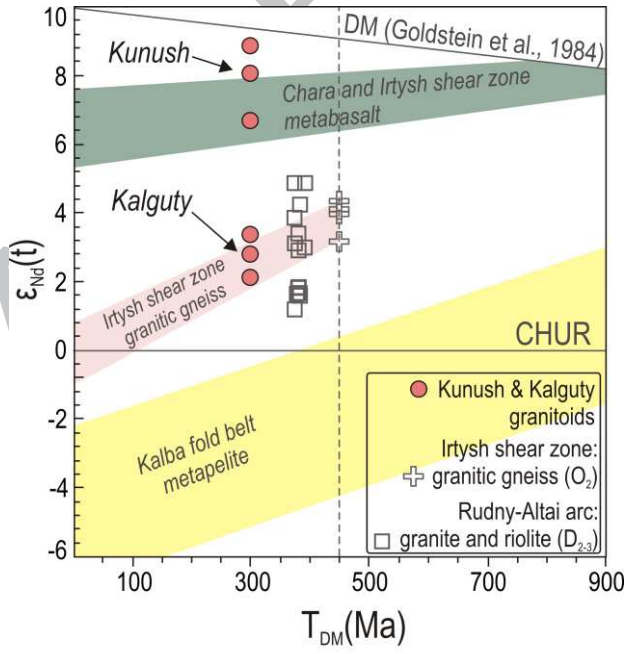

Figure 10.

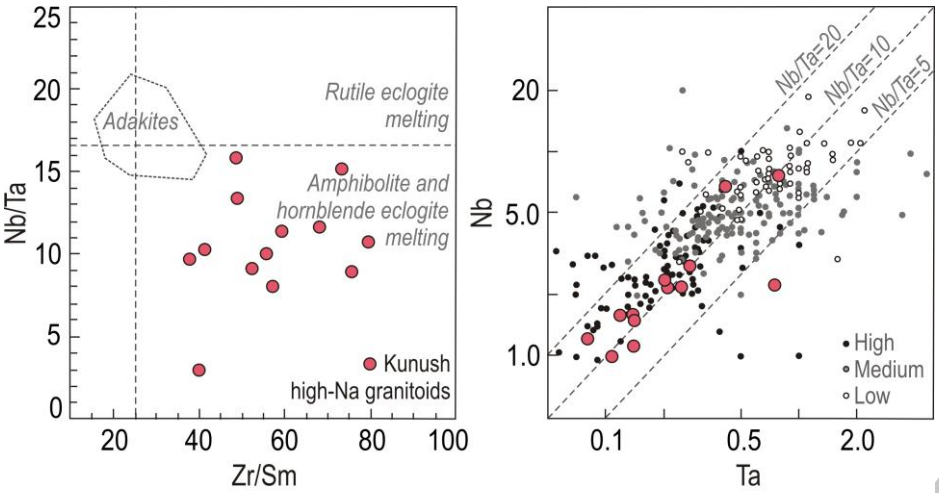

Figure 11.

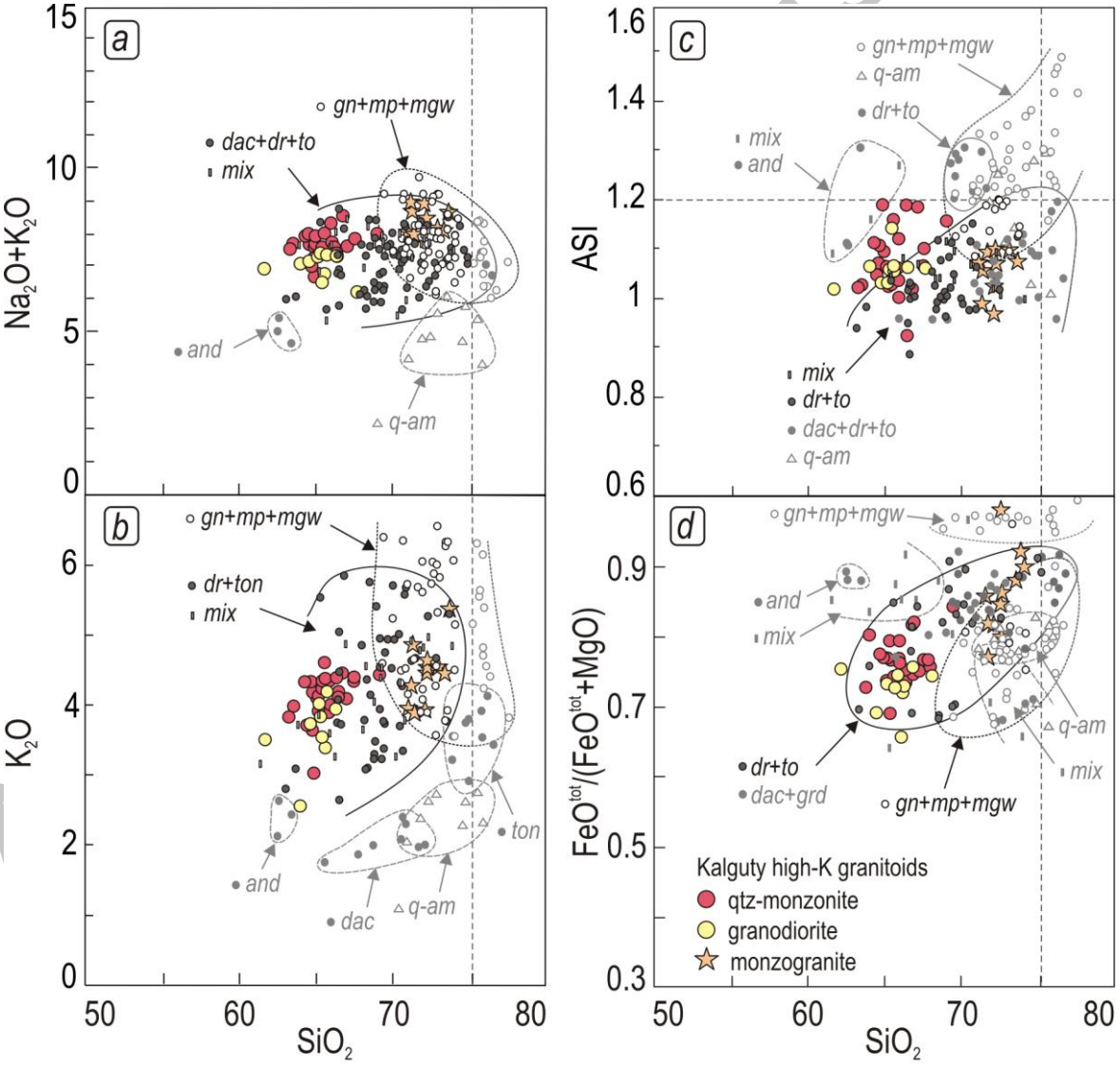

Figure 12.

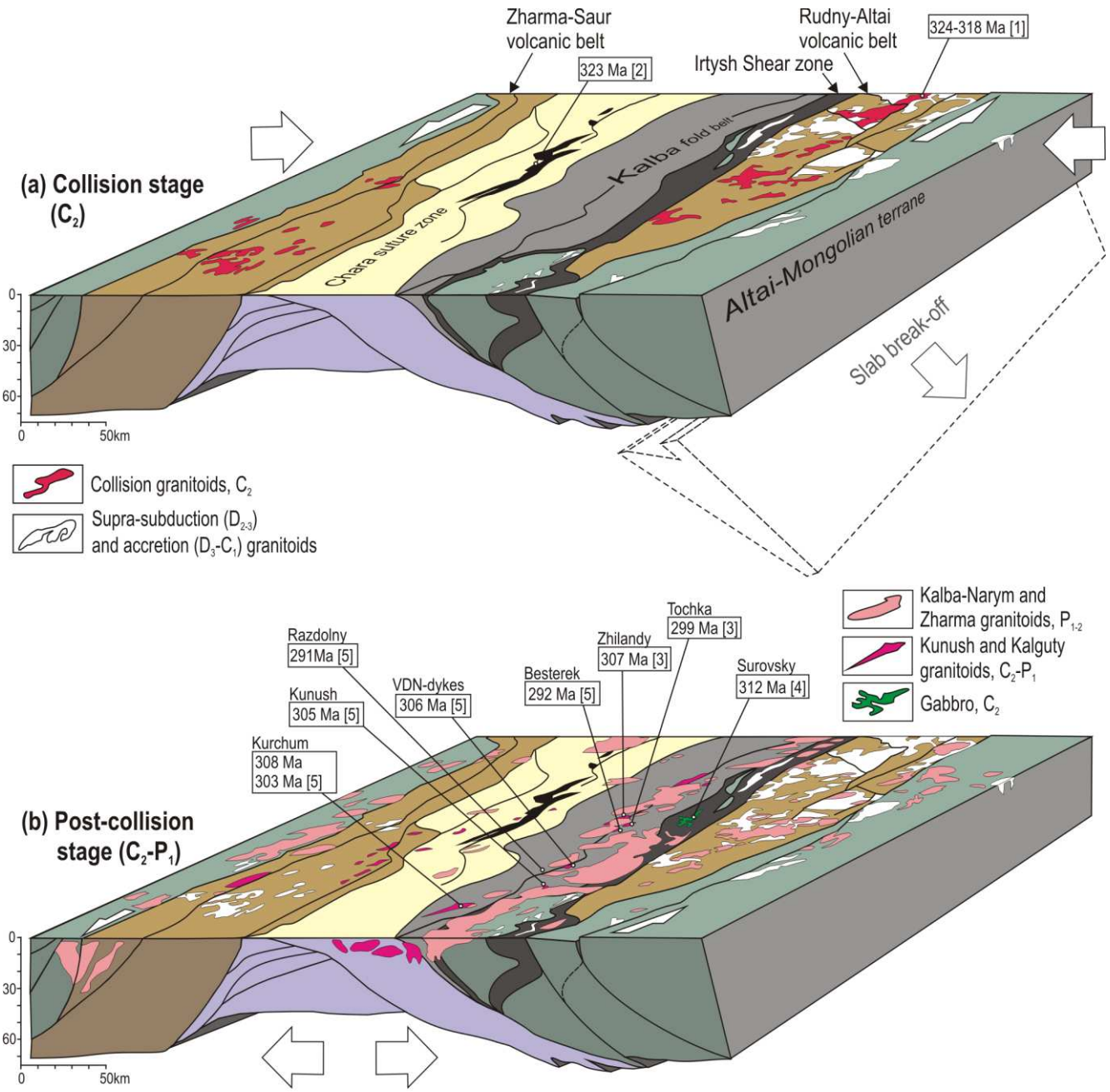

Figure 13.

Table 1. LA-ICP-MS zircon U-Pb isotopic data of the Kunush and Kalguty granitoids (Kalba-Narym fold belt).

No	Point No	Isotope rations, ± 1σ		Rho	Age, Ma, ± 1σ		Discord. %
		$^{207}Pb/^{235}U$	$^{206}Pb/^{238}U$		$^{207}Pb/^{235}U$	$^{206}Pb/^{238}U$	
Kurchum quartz-monzonite. Sample X-1052							
1	1	0.36603±0.01487	0.04991±0.00063	0.31	316.7±11.1	314.0±3.8	0.9
2	2	0.36048±0.01675	0.04955±0.00068	0.30	312.6±12.5	311.8±4.2	0.3
3	3	0.35759±0.02266	0.04820±0.00066	0.22	310.4±16.9	303.5±4.0	2.3
4	5	0.35632±0.02306	0.04913±0.00069	0.22	309.5±17.3	309.2±4.3	0.1
5	6	0.35859±0.02023	0.04843±0.00069	0.25	311.2±15.1	304.9±4.2	2.1
6	7	0.35653±0.02489	0.04838±0.00064	0.19	309.6±18.6	304.6±3.9	1.6
7	8	0.35789±0.03802	0.0492±0.00078	0.15	310.6±28.4	309.8±4.8	0.3
8	9	0.35723±0.01975	0.04924±0.00065	0.24	310.1±14.8	309.9±4.0	0.1
9	10	0.35512±0.02198	0.04913±0.00064	0.21	308.6±16.5	309.2±3.9	-0.2
10	11	0.35569±0.03689	0.04885±0.00081	0.16	309.0±27.6	307.5±5.0	0.5
11	12	0.36440±0.02683	0.04928±0.00066	0.18	315.5±20.0	310.1±4.1	1.7
12	13	0.35664±0.02439	0.04980±0.00075	0.22	309.7±18.3	313.3±4.6	-1.1
13	14	0.36270±0.02684	0.04947±0.00068	0.19	314.2±20.0	311.3±4.2	0.9
14	17	0.34944±0.01597	0.04926±0.00065	0.29	304.3±12.0	310.0±4.0	-1.8
15	18	0.35924±0.02524	0.04866±0.00067	0.20	311.6±18.9	306.3±4.1	1.7
16	19	0.36023±0.01901	0.04893±0.00069	0.27	312.4±14.2	308.0±4.2	1.4
17	20	0.34598±0.05124	0.04915±0.00093	0.13	301.7±38.7	309.3±5.7	-2.5
18	22	0.36111±0.01889	0.04893±0.00065	0.25	313.0±14.1	307.9±4.0	1.7
19	25	0.35759±0.03133	0.04925±0.00081	0.19	310.4±23.4	309.9±5.0	0.2
20	26	0.35297±0.02077	0.04837±0.00074	0.26	307.0±15.6	304.5±4.6	0.8
21	27	0.35613±0.02267	0.04865±0.00074	0.24	309.3±17.0	306.2±4.5	1.0
22	28	0.36287±0.02423	0.04853±0.00064	0.20	314.4±18.1	305.5±4.0	2.9
23	29	0.35990±0.02190	0.04942±0.00067	0.22	312.1±16.4	311.0±4.1	0.4
24	30	0.34485±0.01733	0.04865±0.00065	0.28	300.8±13.1	306.2±4.2	-1.8

25	31	0.36359±0.01773	0.04940±0.00069	0.29	314.9±13.2	310.8±4.3	1.3
26	32	0.34092±0.03194	0.04832±0.00081	0.18	297.9±24.2	304.2±5.0	-2.1
27	33	0.35616±0.01914	0.04922±0.00073	0.28	309.3±14.3	309.7±4.5	-0.1
28	34	0.35203±0.03211	0.04925±0.00080	0.18	306.2±24.1	309.9±4.9	-1.2
29	35	0.35103±0.01889	0.04787±0.00068	0.26	305.5±14.2	301.4±4.2	1.4
30	36	0.35109±0.03154	0.04891±0.00072	0.16	305.5±23.7	307.8±4.4	-0.7
31	37	0.35869±0.02238	0.04934±0.00074	0.24	311.2±16.7	310.5±4.5	0.2
32	38	0.36704±0.03601	0.04910±0.00084	0.17	317.5±26.8	309.0±5.2	2.8
33	39	0.357787±0.04128	0.04903±0.00095	0.17	310.6±30.9	308.6±5.8	0.6
34	40	0.35033±0.02360	0.04876±0.00073	0.22	305.0±17.8	306.9±4.5	-0.6
35	41	0.35173±0.01891	0.04781±0.00071	0.28	306.0±14.2	301.1±4.4	1.6
36	42	0.35984±0.02122	0.04883±0.00074	0.26	312.1±15.9	307.3±4.5	1.6
37	43	0.34328±0.02002	0.04827±0.00075	0.27	299.7±15.1	303.9±4.6	-1.4
38	44	0.35775±0.02159	0.04911±0.00074	0.25	310.5±16.2	309.1±4.5	0.5
39	45	0.36263±0.03546	0.05027±0.00090	0.18	314.2±26.4	316.2±5.5	-0.6
40	46	0.35887±0.01997	0.04915±0.00076	0.28	311.3±14.9	309.3±4.7	0.6
41	47	0.34870±0.01920	0.04827±0.00073	0.27	303.7±14.5	303.9±4.5	-0.1
42	48	0.35991±0.02563	0.04865±0.00076	0.22	312.1±19.1	306.2±4.7	1.9
43	49	0.36316±0.02342	0.04952±0.00077	0.24	314.6±17.4	311.6±4.7	1.0
44	50	0.35390±0.02896	0.04886±0.00082	0.21	307.7±21.7	307.5±5.1	0.1
			Kurchum quartz-monzonite. Sample X-1047				
45	1	0.35359±0.01494	0.04922±0.00061	0.29	307.4±11.2	309.7±3.7	-0.7
46	2	0.34615±0.02220	0.04829±0.00068	0.22	301.8±16.7	304.0±4.2	-0.7
47	3	0.35817±0.02685	0.04745±0.00059	0.17	310.8±20.1	298.9±3.6	4.0
48	4	0.33942±0.02405	0.04780±0.00063	0.19	296.7±18.2	301.0±3.9	-1.4
49	5	0.35830±0.01840	0.04800±0.00066	0.27	310.9±13.8	302.2±4.0	2.9
50	6	0.34385±0.02673	0.04827±0.00057	0.15	300.1±20.2	303.9±3.5	-1.3
51	7	0.34920±0.01164	0.04878±0.00056	0.34	304.1±8.8	307.0±3.4	-0.9
52	9	0.35154±0.01362	0.04761±0.00052	0.28	305.9±10.2	299.8±3.2	2.0

Table 1 (continue)

53	10	0.35744±0.00941	0.04900±0.00052	0.40	310.3±7.0	308.4±3.2	0.6
54	11	0.34621±0.02174	0.04798±0.00063	0.21	301.9±16.4	302.1±3.9	-0.1
55	13	0.33973±0.01795	0.04820±0.00051	0.20	297.0±13.6	303.4±3.2	-2.1
56	14	0.35384±0.00888	0.04825±0.00050	0.41	307.6±6.7	303.8±3.1	1.3
57	15	0.34097±0.01678	0.04720±0.00058	0.25	297.9±12.7	297.3±3.6	0.2
58	16	0.35252±0.02564	0.04841±0.00054	0.15	306.6±19.3	304.8±3.3	0.6
59	17	0.34679±0.01013	0.04703±0.00051	0.37	302.3±7.6	296.3±3.2	2.0
60	18	0.34837±0.01564	0.04805±0.00057	0.26	303.5±11.8	302.5±3.5	0.3
61	20	0.35333±0.01115	0.04805±0.00050	0.33	307.2±8.4	302.5±3.1	1.6
62	22	0.34833±0.02951	0.04830±0.00060	0.15	303.5±22.2	304.1±3.7	-0.2
63	23	0.34717±0.02964	0.04912±0.00062	0.15	302.6±22.3	309.1±3.8	-2.1
64	24	0.36036±0.01181	0.04903±0.00056	0.35	312.5±8.8	308.5±3.4	1.3
65	25	0.34645±0.00996	0.04772±0.00052	0.38	302.1±7.5	300.5±3.2	0.5
66	26	0.34526±0.00971	0.04706±0.00051	0.39	301.1±7.3	296.5±3.1	1.6
67	27	0.34686±0.01708	0.04958±0.00055	0.23	302.4±12.9	311.9±3.4	-3.0
68	28	0.35114±0.01189	0.04775±0.00055	0.34	305.6±8.9	300.7±3.4	1.6
69	29	0.34177±0.02002	0.04876±0.00055	0.19	298.5±15.2	306.9±3.4	-2.7
70	30	0.34945±0.02175	0.04838±0.00055	0.18	304.3±16.4	304.6±3.4	-0.1
71	31	0.34204±0.02436	0.04732±0.00055	0.16	298.7±18.4	298.0±3.4	0.2
72	32	0.35799±0.02773	0.04905±0.00063	0.17	310.7±20.7	308.7±3.9	0.6
73	33	0.36056±0.01506	0.04855±0.00063	0.31	312.6±11.2	305.6±3.9	2.3
74	34	0.36104±0.01351	0.04891±0.00057	0.31	313.0±10.1	307.8±3.5	1.7
75	36	0.36101±0.02829	0.04848±0.00062	0.16	313.0±21.1	305.2±3.8	2.6
			Razdolny granodiorite. Sample MX-841				
76	1	0.35471±0.01195	0.04578±0.00051	0.33	308.3±9.0	288.5±3.1	6.9
77	3	0.34637±0.01438	0.04512±0.00054	0.29	302.0±10.9	284.5±3.4	6.2
78	7	0.30895±0.01529	0.04571±0.00060	0.27	273.4±11.9	288.1±3.7	-5.1
79	8	0.33741±0.00968	0.04741±0.00050	0.37	295.2±7.4	298.6±3.1	-1.1
80	9	0.33656±0.01361	0.04672±0.00056	0.30	294.6±10.3	294.3±3.4	0.1
81	14	0.31167±0.01346	0.04597±0.00056	0.28	275.5±10.4	289.7±3.5	-4.9
82	15	0.34159±0.01391	0.04549±0.00055	0.30	298.4±10.5	286.8±3.4	4.0
83	16	0.31418±0.01283	0.04598±0.00055	0.29	277.4±9.9	289.8±3.4	-4.3

84	17	0.32739±0.01637	0.04606±0.00061	0.26	287.6±12.5	290.3±3.7	-0.9
85	18	0.33912±0.01668	0.04590±0.00060	0.27	296.5±12.7	289.3±3.7	2.5
86	21	0.34872±0.01501	0.04571±0.00057	0.29	303.8±11.3	288.1±3.5	5.4
87	22	0.34677±0.01473	0.04697±0.00057	0.29	302.3±11.1	295.9±3.5	2.2
88	24	0.33710±0.01379	0.04641±0.00056	0.29	295.0±10.5	292.4±3.4	0.9
89	25	0.31454±0.01637	0.04564±0.00062	0.26	277.7±12.6	287.7±3.8	-3.5
90	26	0.33618±0.01641	0.04559±0.00060	0.27	294.3±12.5	287.4±3.7	2.4
91	29	0.32571±0.01517	0.04627±0.00059	0.27	286.3±11.6	291.6±3.7	-1.8
92	30	0.34402±0.01520	0.04672±0.00058	0.28	300.2±11.5	294.4±3.6	2.0
93	31	0.34209±0.01485	0.04668±0.00058	0.29	298.8±11.2	294.1±3.6	1.6
94	32	0.34180±0.01713	0.04710±0.00063	0.27	298.5±13.0	296.7±3.9	0.6
95	34	0.34550±0.01819	0.04609±0.00065	0.27	301.313.7	290.5±4.0	3.7
96	35	0.33185±0.01740	0.04654±0.00064	0.26	291.0±13.3	293.3±3.9	-0.8
97	36	0.34450±0.01796	0.04566±0.00063	0.26	300.6±13.6	287.8±3.9	4.4
98	37	0.34466±0.01875	0.04665±0.00066	0.26	300.7±14.2	293.9±4.1	2.3
99	40	0.35343±0.01770	0.04550±0.00061	0.27	307.3±13.3	286.9±3.8	7.1
			VDN-dyke quartz-monzonite porphyry. Sample KT-34/1				
100	1	0.35761±0.01211	0.04955±0.00050	0.30	310.4±9.1	311.7±3.1	-0.4
101	2	0.34445±0.01624	0.04909±0.00057	0.25	300.5±12.3	308.9±3.5	-2.7
102	3	0.35904±0.01436	0.04859±0.00053	0.27	311.5±10.7	305.9±3.3	1.8
103	4	0.34284±0.01348	0.04855±0.00053	0.28	299.3±10.2	305.6±3.3	-2.1
104	5	0.36808±0.01815	0.04864±0.00059	0.25	318.2±13.5	306.2±3.6	3.9
105	6	0.35778±0.01426	0.04922±0.00053	0.27	310.6±10.7	309.7±3.3	0.3
106	7	0.35898±0.01700	0.04880±0.00060	0.26	311.5±12.7	307.2±3.7	1.4
107	8	0.36134±0.01942	0.04865±0.00063	0.24	313.2±14.5	306.3±3.9	2.3
108	9	0.36063±0.01438	0.04835±0.00052	0.27	312.7±10.7	304.4±3.2	2.7
109	10	0.34772±0.01695	0.04899±0.00059	0.25	303.0±12.8	308.3±3.7	-1.7

Table 1 (continue)

110	11	0.35757±0.01774	0.04876±0.00059	0.24	310.4±13.3	306.9±3.6	1.1
111	12	0.34613±0.01412	0.04835±0.00053	0.27	301.8±10.7	304.4±3.2	-0.9
112	13	0.35297±0.01919	0.04766±0.00062	0.24	307.0±14.4	300.1±3.8	2.3

113	14	0.35918±0.01959	0.04814±0.00059	0.22	311.6±14.6	303.1±3.6	2.8
114	15	0.35549±0.01594	0.04864±0.00055	0.25	308.8±11.9	306.2±3.4	0.8
115	16	0.35601±0.02806	0.04751±0.00062	0.17	309.2±21.0	299.2±3.8	3.3
116	17	0.36676±0.01687	0.04909±0.00056	0.25	317.3±12.5	308.9±3.5	2.7
117	18	0.34738±0.01818	0.04836±0.00060	0.24	302.8±13.7	304.5±3.7	-0.6
118	19	0.36377±0.01763	0.05011±0.00060	0.25	315.0±13.1	315.2±3.7	-0.1
119	20	0.36800±0.01795	0.04768±0.00056	0.24	318.2±13.3	300.2±3.5	6.0
120	22	0.36193±0.01987	0.04779±0.00061	0.23	313.7±14.8	300.9±3.7	4.3
121	24	0.36387±0.01977	0.04793±0.00059	0.23	315.1±14.7	301.8±3.6	4.4
			Kunush-dyke granite porphyry. Sample 7-694				
122	1	0.34822±0.01284	0.04781±0.00072	0.41	303.4±9.7	301.0±4.4	0.8
123	2	0.34358±0.01096	0.04792±0.00065	0.43	299.9±8.3	301.8±4.0	-0.6
124	5	0.35386±0.01241	0.04868±0.00071	0.42	307.6±9.3	306.4±4.4	0.4
125	7	0.34882±0.01450	0.04823±0.00079	0.39	303.8±10.9	303.6±4.9	0.1
126	8	0.34775±0.01206	0.04845±0.00070	0.42	303.0±9.1	305.0±4.3	-0.7
127	9	0.35271±0.00961	0.04858±0.00061	0.46	306.8±7.2	305.8±3.8	0.3
128	10	0.36628±0.01539	0.04979±0.00082	0.39	316.9±11.4	313.2±5.1	1.2
129	13	0.34770±0.01321	0.05003±0.00076	0.40	303.0±10.0	314.7±4.7	-3.7
130	15	0.36065±0.01247	0.05019±0.00073	0.42	312.7±9.3	315.7±4.5	-1.0
131	18	0.36866±0.01559	0.04993±0.00084	0.40	318.7±11.6	314.1±5.1	1.5
132	24	0.33436±0.01340	0.04743±0.00076	0.40	292.9±10.2	298.7±4.7	-1.9
133	26	0.36118±0.02235	0.04905±0.00109	0.36	313.1±16.7	308.7±6.7	1.4
134	29	0.35739±0.02054	0.04957±0.00104	0.37	310.3±15.4	311.9±6.4	-0.5
135	30	0.35158±0.01824	0.04850±0.00095	0.38	305.9±13.7	305.3±5.8	0.2
136	22	0.33985±0.01318	0.04643±0.00073	0.41	297.1±10.0	292.6±4.5	1.5
137	25	0.33186±0.01561	0.04613±0.00083	0.38	291.0±11.9	290.7±5.1	0.1
138	28	0.34333±0.02036	0.04611±0.00100	0.37	299.7±15.4	290.6±6.2	3.1
139	20	0.39033±0.01525	0.05285±0.00084	0.41	334.6±11.1	332.0±5.1	0.8
140	14	0.39899±0.02134	0.05455±0.00108	0.37	340.9±15.5	342.4±6.6	-0.4
141	19	0.39617±0.03719	0.05459±0.00132	0.26	338.9±27.1	342.7±8.1	-1.1
142	16	0.37016±0.02010	0.05494±0.00107	0.36	319.8±14.9	344.8±6.5	-7.3
143	21	0.43773±0.01471	0.05830±0.00084	0.43	368.6±10.4	365.3±5.1	0.9

144	6	0.47189±0.02574	0.06041±0.00125	0.38	392.5±17.8	378.1±7.6	3.8
145	11	0.47111±0.01926	0.06232±0.00103	0.40	392.0±13.3	389.7±6.2	0.6
146	23	0.51143±0.01863	0.06481±0.00099	0.42	419.4±12.5	404.8±6.0	3.6
147	12	0.64205±0.02037	0.08398±0.00117	0.44	503.6±12.6	519.8±7.0	-3.1
148	3	1.31475±0.03091	0.14044±0.00169	0.51	852.2±13.6	847.1±9.6	0.6
149	17	1.41836±0.06220	0.15427±0.00292	0.43	896.7±26.1	924.8±16.3	-3.0
150	27	2.28719±0.09115	0.19957±0.00349	0.44	1208±28.2	1173±18.8	3.0
151	24	0.33436±0.01340	0.04743±0.00076	0.40	292.9±10.2	298.7±4.7	-1.9
			Besterek porphyritic granite. Sample K-14-104				
152	2	0.34007±0.00685	0.04656±0.00042	0.45	297.2±5.2	293.4±2.6	1.3
153	3	0.33123±0.00638	0.04617±0.00041	0.46	290.5±4.9	290.9±.5	-0.1
154	6	0.35128±0.00640	0.04747±0.00042	0.49	305.7±4.8	298.9±2.6	2.3
155	8	0.32843±0.00834	0.04598±0.00044	0.38	288.4±6.4	289.8±2.7	-0.5
156	9	0.33795±0.00741	0.04685±0.00043	0.42	295.6±5.6	295.2±2.6	0.1
157	11	0.32820±0.00695	0.04656±0.00042	0.43	288.2±5.3	293.4±2.6	-1.8
158	15	0.33985±0.01364	0.04749±0.00055	0.29	297.1±10.3	299.1±3.4	-0.7
159	16	0.33772±0.00697	0.04584±0.00041	0.43	295.4±5.3	288.9±2.6	2.2
160	20	0.33488±0.00626	0.04732±0.00042	0.47	293.3±4.8	298.0±2.6	-1.6
161	21	0.32543±0.00691	0.04569±0.00041	0.42	286.1±5.3	288.0±2.6	-0.7
162	27	0.33519±0.00697	0.04629±0.00042	0.44	293.5±5.3	291.7±2.6	0.6
163	28	0.31892±0.00816	0.04617±0.00044	0.37	281.1±6.3	290.9±2.7	-3.4
164	29	0.33053±0.00794	0.04666±0.00043	0.38	290.0±6.1	294.0±2.7	-1.4
165	30	0.32999±0.00810	0.04542±0.00043	0.39	289.6±6.2	286.3±2.6	1.2
166	31	0.33539±0.00635	0.04712±0.00042	0.47	293.7±4.8	296.8±2.6	-1.0

Table 1 (continue)

167	32	0.33169±0.00783	0.04527±0.00042	0.39	290.9±6.0	285.4±2.6	1.9
168	33	0.33159±0.00529	0.04654±0.00040	0.54	290.8±4.0	293.3±2.5	-0.9
171	36	0.33386±0.00839	0.04625±0.00044	0.38	292.5±6.4	291.4±2.7	0.4
172	37	0.32176±0.00605	0.04586±0.00041	0.48	283.3±4.7	289.1±2.5	-2.0
173	40	0.33492±0.00690	0.04601±0.00041	0.43	293.3±5.3	290.0±2.6	1.1

Table 2. Major oxides (wt.%) and trace elements (ppm) in the high-Na Kunush granitoids.

Rock	Massive granite		Porphyritic granite							Granite-porphyry and fine-grained type			
Intrusion	Zhilandy		Tochka				Kunush	Besterek		Zhilandy	Tochka	Kunush	Razdolny
№	7-181	7-180/1	7-187	7-185	7-236	7-182	7-691-1	MX-223	K14-105/1	7-174	7-183	7-694	X -1031
SiO_2	69.6	69.92	68.31	68.75	69.24	71.16	71.1	70.71	71.98	68.06	70.27	71.38	68.11
TiO_2	0.24	0.24	0.13	0.13	0.13	0.23	0.27	0.13	0.11	0.55	0.24	0.24	0.4
AL_2O_3	16.35	15.97	18.36	17.26	18.22	15.96	15.74	16.75	15.14	16.48	15.46	15.32	15.48
Fe_2O_3*	2.33	2.54	1.91	1.43	1.65	1.67	2	1.8	1.6	3.17	2.37	2.06	3.42
MnO	<0.03	0.03	0.04	<0.03	<0.03	<0.03	0.03	0.03	0.02	0.05	<0.03	0.03	0.06
MgO	1.14	1.18	0.99	1.19	0.84	1.16	0.77	0.85	0.59	1.32	1.14	0.77	1.19
CaO	2.96	3.06	4.12	3.88	4.03	3.27	2.62	3.56	2.17	3.10	3.09	2.67	3.27
Na_2O	4.82	4.81	4.5	5.85	4.27	4.79	5.49	5.13	5.12	4.73	5.65	5.7	4.1
K_2O	1.26	1.55	0.7	0.96	0.85	1.22	1.03	0.93	1.79	1.57	1.69	1.19	2.11
P_2O_5	0.07	0.06	0.04	0.04	0.05	0.06	0.09	0.06	0.04	0.15	0.07	0.09	0.11
LOI	0.92	0.78	0.5	0.19	0.35	0.49	0.82	0.66	0.52	0.68	0.2	0.5	1.3
SUM	99.7	100.15	99.6	99.69	99.64	100.04	100.04	99.96	99.17	99.9	100.19	100.04	99.61
ASI	1.13	1.07	1.19	0.99	1.21	1.07	1.08	1.07	1.08	1.11	0.94	1	1.05
Mg#	49	48	51	62	50	58	43	48	42	45	49	43	41
Th	1.8	2.1	0.7	1.2	1.4	1.9	2.6	0.8	3.1	5.85	3.54	2.6	6.1
U	0.47	0.54	0.54	1	1.01	0.45	3.67	0.33	0.8	1.81	0.92	1.68	2.14
Rb	23	27	22	32	20	21	62	21	28	52	31	62	69
Ba	256	283	203	221	202	254	198	201	515	414	276	226	400
Sr	727	620	565	681	754	682	430	558	407	659	551	418	511
La	7.7	10.3	3.2	4.5	5.4	7.8	12.9	4.2	7.4	21.9	10.8	14.6	16.6
Ce	16	22	6	10	12	17	25	9	16	40	21	27	33
Pr	2.2	3	0.9	1.3	1.6	2.4	3.1	1.1	2.3	5.1	2.9	3.4	3.7
Nd	8.7	11.6	3.8	5.7	7.1	9.4	11.1	4.6	9.6	18.9	10.7	11.8	14.5
Sm	1.7	2.4	0.9	1.2	1.5	1.8	1.9	0.9	2.2	3.4	2	2	3.1
Eu	0.58	0.51	0.29	0.36	0.49	0.55	0.54	0.22	0.77	1.09	0.64	0.54	0.78
Gd	1.32	1.64	0.7	0.94	1.02	1.28	1.57	0.77	2	2.59	1.48	1.79	2.29
Tb	0.2	0.2	0.11	0.13	0.13	0.17	0.19	0.11	0.3	0.33	0.19	0.25	0.36
Dy	0.92	1.06	0.53	0.66	0.76	0.79	0.83	0.59	1.56	1.79	0.97	1.08	1.98
Ho	0.15	0.19	0.1	0.13	0.13	0.16	0.13	0.11	0.28	0.32	0.16	0.19	0.34
Er	0.45	0.58	0.26	0.32	0.38	0.43	0.38	0.27	0.74	0.89	0.44	0.44	1
Tm	0.07	0.09	0.04	0.05	0.06	0.07	0.06	0.04	0.11	0.13	0.06	0.06	0.15
Yb	0.39	0.59	0.26	0.33	0.38	0.39	0.32	0.22	0.65	0.79	0.38	0.38	0.93
Lu	0.07	0.08	0.04	0.05	0.05	0.06	0.05	0.03	0.09	0.13	0.06	0.06	0.13
Zr	102	98	69	69	78	86	144	68	88	168	113	138	117
Hf	2.8	3	2	2.2	2.4	2.4	3.9	1.7	3.2	4.11	3.04	3.8	4
Ta	0.14	0.21	0.14	0.14	0.11	0.12	0.24	0.08	0.75	0.42	0.27	0.2	0.78
Nb	1.6	2.2	1.5	1.1	1	1.6	2.2	1.2	2.2	6.6	2.7	2.3	7.5
Y	5	6	3	4	4	5	5	4	9	10	5	6	11
V	7	4	5	4	5	3	8	7	6	12	6	4	8
Cr	39	14	6	8	9	12	14	11	34	16	12	9	10
Ni	27	20	24	26	14	12	19	19	5	26	11	12	20
Eu/Eu*	1.1	0.7	1.1	1.0	1.1	1.1	0.9	0.8	1.1	1.1	1.1	0.8	0.9
La/Yb_N	13	12	8	9	10	14	27	13	8	19	19	26	12
Sr/Y	151	101	177	182	179	143	85	134	47	67	110	66	46
ΣРЗЭ	41	54	17	25	31	42	58	22	44	97	52	64	78

Table 3. Major oxides (wt.%) and trace elements (ppm) in the high-K Kalguty granitoids.

Rock	Early Qtz-monzonite		Late Qtz-monzonite	Final monzogranite		Qtz-monzonite porphyry		Granodiorite					
Intrusion	Kurchum		Kurchum	Kurchum		VDN-dike		Razdolny					
№	X-1052	X-1051	X-1047	X-1049	X-1053	KT-34/1	X-1170	X-1032	X-1033	X-1036	MX-839	MX-840	MX-841
SiO_2	65,16	66,39	66,14	72,66	74,17	69,48	66,89	62,22	65,15	66,84	65,78	65,72	66,17
TiO_2	0,78	0,83	0,63	0,17	0,2	0,55	0,60	1,02	0,8	0,64	0,8	0,82	0,83
AL_2O_3	16	15,81	15,33	13,62	13,19	15,34	15,57	15,91	15,59	15,25	15,58	15,72	15,86
$Fe_2O_3^*$	5,09	4,56	4,49	2,39	2,08	4,11	4,85	6,81	5,1	4,57	4,73	4,83	4,79
MnO	0,08	0,1	0,07	0,04	0,03	0,06	0,08	0,1	0,08	0,07	0,14	0,07	0,07
MgO	1,84	1,68	1,48	0,39	0,24	0,78	1,08	2,22	1,88	1,47	1,77	1,76	1,85
CaO	2,86	2,48	2,64	0,77	0,78	1,77	2,08	3,76	3,3	2,78	2,98	3,22	3,19
Na_2O	3,4	3,3	3,43	3,85	3,26	3,5	3,35	3,39	3,41	3,35	3,33	3,47	3,17
K_2O	4,29	4,32	4,35	4,56	5,33	4,44	4,09	3,47	3,69	3,93	4,01	3,8	4,17
P_2O_5	0,17	0,19	0,31	0,04	0,05	0,22	0,18	0,22	0,19	0,17	0,18	0,18	0,2
LOI	0.75	1.22	1.18	1.6	0.55	0.52	1.22	1.08	1.1	0.98	0,32	0,18	0,29
SUM	100,53	100,87	100,13	100,13	99,92	100,83	100	100,35	100,3	100,04	99,73	99,87	100,69
ASI	1,03	1,08	1,01	1,07	1,05	1,11	1,13	0,98	1	1,03	1,02	1	1,02
*Fe**	0,73	0,73	0,75	0,86	0,9	0,84	0,82	0,75	0,73	0,76	0,73	0,73	0,72
Th	15,3	15	19,3	16,2	23,2	10,7	15	11,2	15,3	19,1	13,8	14,2	16,8
U	3,02	3,56	4,77	4,69	6,67	3,46	3,73	4,38	3,71	2,39	3,75	3,96	3,11
Rb	148	160	148	199	227	182	137	122	148	158	120	117	115
Ba	482	474	357	89	160	421	557	476	454	433	410	386	410
Sr	222	214	194	37	48	176	187	307	294	271	242	253	264
La	36,1	38,9	36,3	17,5	43,3	32,9	25,46	34,8	42,1	49,8	28,5	32,6	20,7
Ce	76	79	76	38	90	66	52	73	84	95	59	67	41
Pr	9	9,4	8,6	4,8	10,1	7,8	8,39	8,4	9,5	10,4	7,7	8,7	5,9
Nd	37,1	38,3	35,1	19,5	38,7	28,5	34,47	34,5	37,9	40,6	29,1	32,7	22,8
Sm	7,4	7,7	7,6	5,3	8,3	5,9	7,58	7,2	7,7	7,5	6	6,5	5,2
Eu	1,05	1,05	0,9	0,23	0,27	0,71	1,29	1,4	1,21	1,05	1,02	1,06	1,05
Gd	6,62	7,54	6,9	5,7	7,2	4,95	7,03	6,48	6,72	6,15	6,94	7,06	6,24
Tb	1,13	1,18	1,12	1,02	1,18	0,82	1	1	1,02	0,9	1,05	1,01	0,96
Dy	6,82	7,14	6,87	6,83	7,41	4,34	5,74	6,1	6	5,08	5,91	5,78	5,62
Ho	1,26	1,44	1,31	1,28	1,47	0,82	1,05	1,16	1,16	0,94	1,2	1,16	1,14
Er	3,78	3,88	3,87	3,87	4,43	2,24	3,07	3,29	3,31	2,72	3,3	3,31	3,46
Tm	0,56	0,6	0,57	0,6	0,66	0,33	0,49	0,45	0,51	0,39	0,54	0,54	0,54
Yb	3,2	3,47	3,4	4,03	4,12	2,1	2,98	3	2,86	2,5	3,36	3,34	3,29
Lu	0,5	0,51	0,5	0,57	0,6	0,28	0,47	0,4	0,42	0,36	0,5	0,51	0,51
Zr	385	366	316	140	182	208	312	335	312	258	237	249	243
Hf	9,2	8,6	7,9	5,5	6	4,5	8,68	8	8,1	6,9	8	8,3	8,1
Ta	0,89	0,99	0,9	1,65	1,14	0,82	1,11	1,12	1,2	1,05	1,26	1,25	1,19
Nb	14	15	13,1	15,1	12,5	13	12,99	15,8	15,5	14,3	12,6	12,9	12,9
Y	41	44	42	44	48	32	35	36	35	29	26	26	26
V	32	4	13	12	20	6	6	14	21	19	20	18	16
Cr	41	10	19	24	37	9	18	15	43	24	15	16	15
Ni	46	14	20	20	31	17	19	18	34	23	14	16	14
Eu/Eu*	0,4	0,4	0,4	0,1	0,1	0,4	0,5	0,6	0,5	0,5	0,5	0,5	0,6
La/Yb_N	8	8	7	3	7	11	6	8	10	13	6	7	4
ΣРЗЭ	190	201	189	110	217	157	151	181	204	224	154	171	118

Table 4. Sm-Nd isotopic compositions for representative samples of the Kunush and Kalguty granitoids.

Sample	Rock	Sm	Nd	$^{147}Sm/^{144}Nd$	$^{143}Nd/^{144}Nd$	Err (2σ)	$E_{(Nd)}0$	$E_{(Nd)}$-t	T_{DM} (Ma)	T_{DM-2} (Ma)
7-181	Massive granite	1,81	8,85	0,122600	0,512834	0,000006	3,82	6,7	532	525
7-694	Granite-porphyry	2,26	11,05	0,123862	0,512905	0,000009	5,21	8,0	418	413
K-14-105/1	Porphyritic granite	1,01	4,37	0,140136	0,512982	0,000010	6,71	8,9	351	340
MX-841	Granodiorite	5,40	22,28	0,146545	0,512682	0,000008	0,86	2,8	1066	849
X-1047	Qtz-monzonite	7,26	34,50	0,127300	0,512672	0,000007	0,67	3,3	846	804
X-1052	Qtz-monzonite	7,29	34,13	0,129076	0,512681	0,000015	0,84	3,4	848	795
KT-34/1	Qtz-monzonite	6,61	30,09	0,132872	0,512620	0,000011	-0,35	2,1	1002	906

Graphical abstract

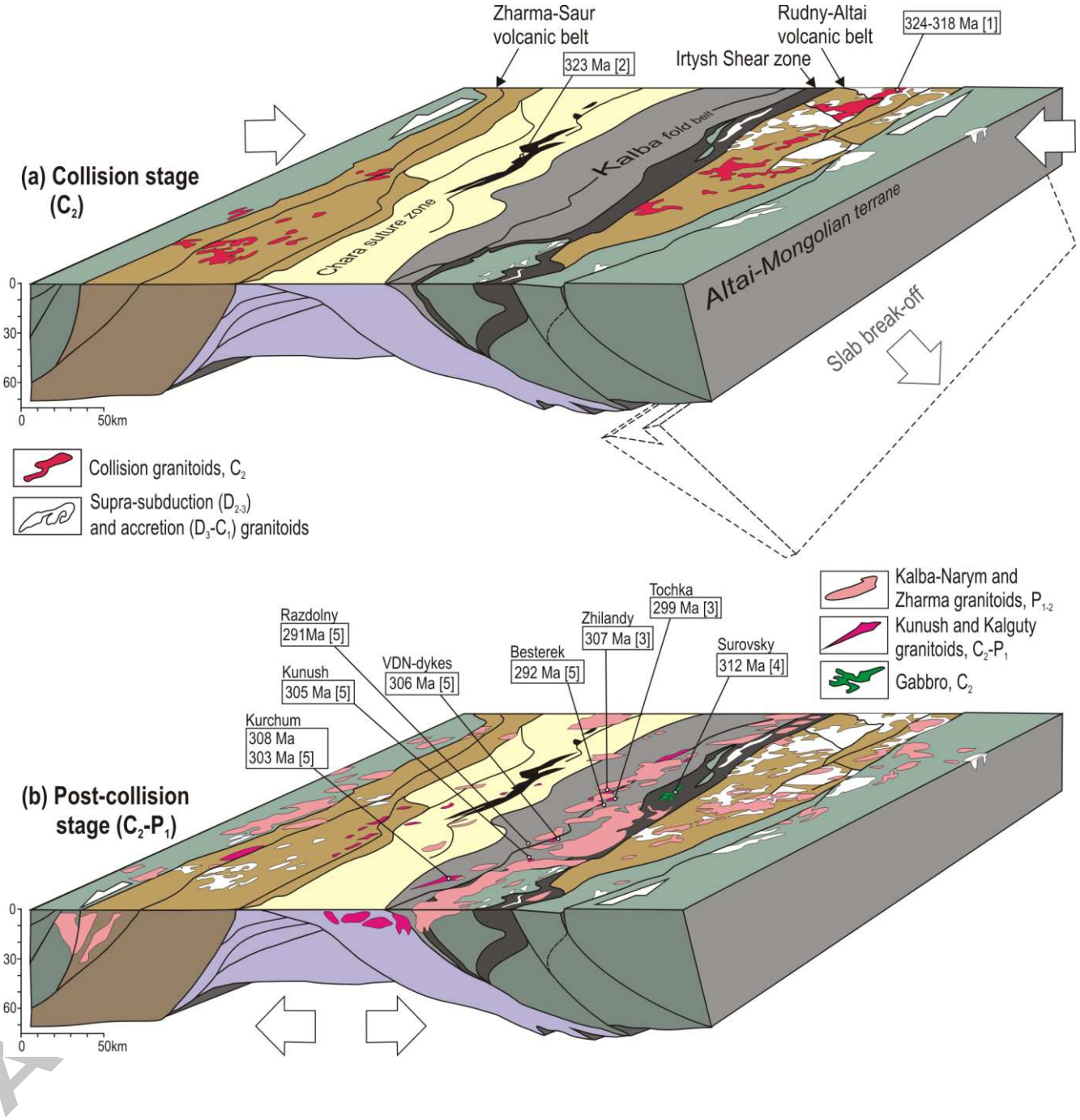

Highlights

The Kunush high-Na and Kalguty high-K granitoids of the Irtysh-Zaisan orogen emplaced synchronously (308-291 Ma) into the Kalba fold belt.

The granitoids were synchronously derived at different depths from metabasaltic (MORB; P = 10-15 kbar) and metagranitic (TTG; P < 10 kbar) protoliths, respectively.

The large-scale melting is recorded in magmatic column of chemically different granitoids, which were generated coevally with the post-orogenic magmatic peak at ~300 Ma.